Author Version: Int. J. Earth Sci. (Geol. Rundsch), vol.105(3); 2016; 905-920

Morphotectonic and Petrological variations along the Southern Central Indian Ridge

Ranadhir Mukhopadhyay*[1], Sridhar D Iyer[1], Dwijesh Ray[2],
S M Karisiddaiah[1], Rajendra K Drolia[3]

[1] CSIR-National Institute of Oceanography, Dona Paula 403004, Goa, India
[2] PLANEX, Physical Research Laboratory, Ahmadabad 380009, India
[3] Formerly with CSIR-National Geophysical Research Institute, Hyderabad 500007, India

**Corresponding Author-Tel: 91-832-245-0246, Fax: 91-832-245-0616, Email: ranadhir@nio.org*

Abstract

In order to ascertain the effect of geomorphic and tectonic domains on the formation, enrichment and ascension of the ridge axis melt, structural and petrological data from a nearly 300 km long axial stretch along the slow to intermediate spreading (40-60 mm/yr) southern Central Indian Ridge (SCIR) was studied. The stretch, approximately between 20°30'S and 23°07'S, was disturbed by two major tectonic features- Egeria Transform Fault (ETF) in the north and the Gemino Fracture Zone (GFZ) in the south- besides eight other discontinuities of variable dimensions. This stretch was chosen to test the petrological variations and mechanisms of magma supply in four distinct geomorphic and tectonic regimes: a Ridge Crest-Flank-Valley (RCFV), a Neo-Volcanic Zone (NVZ), a Large Transform Discontinuity (LTD), and an Overlapping Spreading Center (OSC).

The major and trace element geochemistry of 44 glass and 47 whole rocks, extent and depth of melting (Na_8 and Fe_8, respectively) and melt pristinity (Mg#) of the magma indicate that rocks along this stretch were probably sourced from a reasonably primitive melt generated at a relatively greater depth and later got accumulated in pockets at a shallower level before eruption. Petrochemical analysis and isotopic composition and ratios suggest that in contrast to largely N-MORB type of rocks at RCFV and OSC areas, the rocks from LTD and NVZ locations show signatures of enrichment to transitional (T) and enriched (E) type basalts. A model explaining possible processes of enrichment and ascending framework of the melt at different tectonic regimes along SCIR are discussed.

Keywords: Southern Central Indian Ridge, Overlapping spreading centre, Neo-volcanic zone, Ridge-Transform fault intersection, ascending magma framework

Introduction

The primary geodynamic factor responsible for the crustal accretion processes at the mid-ocean ridges (MOR) is the spreading rate (Purdy et al., 1992), which influences the along- and across-axes bathymetry (Briais, 1995) and petrology (Klein and Langmuir, 1987; Niu and Batiza, 1993). In fact, the petrology and geochemistry of erupted lavas can be useful in understanding the magma chamber dynamics and melting conditions beneath the MOR (Rotella et al., 2009). Several features distinguish the slow spreading ridge (SSR, spreading rate 20-30 mm/yr; e.g., Mid Atlantic Ridge-MAR) from the fast spreading ridge (FSR, 50-80 mm/yr; e.g., East Pacific Rise- EPR; Iyer and Ray, 2003). In contrast to relatively shallow axial valley along FSR, the SSRs are characterized by deep axial valley, segmented by major transform (fracture zone) and/or minor non-transform ridge axis discontinuities creating oblique basins and en-echelon structures (Purdy et al., 1992). Along-axis gravity values show three dimensional buoyancy-driven diapiric upwelling below the SSR and two dimensional plate-driven upwelling below the FSR (Lin and Phipps-Morgan, 1992). Parameters such as mantle temperature, thermal flux and tectonic stress on a local scale may also control the nature and magma supply geometry of the MOR and generation of new crust (Batiza et al., 1988; Niu and Batiza, 1993).

The axial stretch along MOR is often dissected by major fracture zones (FZ); transform faults (TF), and discontinuities of various dimensions depending on distance of separation of two corresponding segments along the discontinuity. These axial discontinuities could also profoundly affect along-axis variation in ridge petrology (Langmuir et al., 1986; Klein and Langmuir, 1987; Batiza et al., 1988; Mukhopadhyay and Iyer, 1993; Ray et al., 2007, 2008). Such discontinuities may result in lowering of magma temperature, high pressure fractionation and smaller extent of melting causing eruption of rocks of variable composition in the proximity (Natland, 1980; Gregg et al., 2009). However, the relationships of finer scale tectonics with the mechanism of magma supply at the secondary discontinuities, and petrological variations within a small segment due to intra-segment variability of melting temperature are yet to be fully understood.

The Central Indian Ridge (CIR) demarcates the present day accretionary boundary of the African-Australian and African-Indian plates, and spans between the Indian Ocean Triple Junction (IOTJ at 25°S, 70°E) and 2°S, where it meets the southern end of the Carlsberg Ridge (CR; Natland, 1980; Mukhopadhyay and Iyer, 1993; inset of Fig. 1). The entire length of the CIR displays a rugged topography with a variable spreading rate (Mukhopadhyay and Iyer, 1993). The northern CIR, for example, occurring between the equator and 10ºS spreads at a rate of 60-84 mm/yr (Drolia et al., 2000), while its southern extension SCIR spans between 10°S and the triple junction located at 25°S

and spreads at a rate of 84-108 mm/yr (full rate, Tapscott et al., 1980; DeMets et al., 2005). Morphology, regional physiographic, magnetic anomalies and kinematic evolution of this slow to intermediate spreading CIR since 42 Ma was studied (Drolia et al., 2000). Using GLORIA long range side-scan sonar and the multibeam swath echo-sounder, Parson et al. (1993) and Briais (1995) mapped the segmentation of the southern CIR (SCIR, ~ 12°S to 25.5°S) to study its morphotectonic characteristics. Petrologically, the SCIR is characterized by N-MORB, gabbro and ultramafics, including serpentized peridotites, talc-anthophyllite, and lherzolites (Engel and Fisher, 1975; Herzig and Plüger, 1988; Ray et al., 2007, 2008).

In this communication, we focus on the morphotectonic features and petrological characteristics of the SCIR between 20°S and 23°S, an area approximately bounded by two major discontinuities- Egeria Transform Fault (ETF) in the north and Gemino Fracture Zone (GFZ) in the south- and several other intervening smaller discontinuities (Fig. 1, *also see footnotes of Table 1*). The data provide an opportunity to address several questions concerning the accretionary processes along the SCIR. These include relationship between petrological and geochemical variations in rocks occurring in various tectonic and geomorphic domains, and the structural framework that allowed ascension of the melt.

Materials and Methods

We acquired underway multibeam swath bathymetry data (beams with 15.5 kHz frequency, Krupp-Atlas make) from the slow to intermediate spreading (40-60 mm/yr) stretch of the south Central Indian Ridge (SCIR) approximately between latitudes 20°30'S and 23°07'S (study area) onboard four cruises- RV Sonne (SO-28, SO-43) and ORV Sagar Kanya (SK-16 and SK-20). To this primary data set, we added morphotectonic observations of several earlier workers to construct the detail background of the study area (Herzig and Plüger, 1988; Chaubey et al., 1990; Mukhopadhyay and Iyer, 1993; Parson et al., 1993; Briais, 1995; Mukhopadhyay et al., 1998; Mudholkar, 2001; DeMets et al. 2005). As many as nine well-developed ridge segments (A to I), separated by ten discontinuities (D1 to D10) were encountered along the stretch of the study area (Table 1). A detailed tectonic and geomorphic analysis of the study area was carried out (Figs. 1 and 2)

Forty-seven basaltic samples from 12 sites were recovered from the study area through dredging (dredging length varying between 2 and 3.5 km) and were geochemically analyzed. These samples came from two geomorphic domains (Ridge-Crest-Floor-Valley [RCFV] and Neo Volcanic Zone [NVZ]), and two tectonic domains (Large Transform discontinuities [LTD] and Overlapping Spreading Centre [OSC], Fig. 1, Table 1). Of the 12 sites, four (74, 77, 78, 80) were located in the

OSC, while samples from two sites (88 and 87) were dredged from the NVZ. While site 91 occurs on a LTD (D2) that separates segment B from A, the rest five sites (66, 85, 90, 93 and 94) occur along the geomorphic domain characterized by inner axial valley and floor along the rift axis (RCFV; Tables 1 and 2).

Using an X-ray Fluorescence, ten major oxide elements (SiO_2, TiO_2, Al_2O_3, Fe_2O_3, MnO, MgO, CaO, Na_2O, K_2O and P_2O_5) of 47 whole rocks from the SCIR were determined (Table 3). A CAMECA electron microprobe was used to analyze 44 fresh basaltic glass cover on these rock tops (Table 4, also see supplementary tables). The concentrations of fourteen trace elements (Nb, Zr, Y, U, Rb, Th, Pb, Co, Mn, Cr, V, Zn, Ni and Cu) were determined in basalts from nine sites in the study area following conventional methods (see Mahoney et al., 1991). The values are shown in table 5. The Fe_8 and Na_8 of the analyzed basalts were estimated to understand the melt characteristics (depth and extent of melting respectively) and Mg # to assess the degree of fractionation, following the equation of Batiza et al. (1988) and Niu and Batiza (1993), where MgO values must be in the range of 5-8% and FeO is considered as total Fe:

- Na_8 (Extent of melting) = $Na_2O+0.373*(MgO) - 2.98$
- Fe_8 (Depth of melting) = $FeO+1.664*(MgO) - 13.313$
- Mg# (Fractionation index) = $100 \times moleMgO / mole(MgO+FeO)^{T,}$ where FeO^T = FeO as total iron

Samples from six sites (RCFV- 90, 93, 94, OSC- 74, NVZ- 87, and LTD- 91) were also analyzed for isotopic composition (Table 6). The isotopic concentration and ratios in these samples were measured by mass-spectrometer on the VG Sector multi-collector instrument at the Hawaii Institute of Geophysics, following a sequential, three-step ion-exchange column procedure of Mahoney et al. (1991). About 20-40 mg of sample was dissolved, each sample was split, and one aliquant spiked with ^{206}Pb, ^{86}Sr, and ^{87}Rb tracers. Pb was then separated from both spiked and un-spiked splits in a two-step elution with mixed HBr-HNO_3 solutions on 50µl anion exchange columns. The wash from the spiked split was loaded onto a 0.6 x 20 cm cation exchange column; Rb and Sr were eluted with 2N HCl (Galer and O'Nions, 1989). Total procedural blanks were nearly negligible (10-40 pg for Pb, and < 200 pg for Sr). Strontium was analyzed in the dynamic multi-collector mode with about 600-800 ng on Ta single filaments with Ta_2O_5 substrate. Pb was run on single Re filaments with silica gel evaporator and H_3PO_4. The spiked fraction was analyzed first to determine concentration, and then 4-8 ng of the unspiked aliquant were loaded and measured for isotopic composition either in single

collector or static multi-collector mode. Two such runs were made for many of the samples (Table 6).

The isotopic fractionation correction remain as $^{86}Sr/^{87}Sr = 0.1194$. Present data are reported relative to Hawaii Institute of Geophysics standard values: for NBS 987 Sr, $^{87}Sr/^{86}Sr = 0.71025$, and for E & A Sr, $^{87}Sr/^{86}Sr = 0.70803$. Pb isotopic ratios were corrected for fractionation using the NBS 981 standard values (Mahoney et al., 1991) and the total ranges measured are ± 0.007 for $^{206}Pb/^{204}Pb$, ± 0.008 for $^{207}pb/^{204}pb$, and ± 0.028 for $^{208}pb/^{204}Pb$. Lead and strontium isotopic ratios from the Indian Ocean Triple Junction (about 200 km south of discontinuity D9), additional samples of study area from Sonne expeditions, and CIR samples from other sources are also included in Table 6 for reference.

Geomorphic and Tectonic Domains

On integration of the analyzed multibeam swath bathymetry data of the present study (SO-28, SO-43, SK-16 and SK-20 cruise data) with that of earlier workers (Herzig and Plüger, 1988; Chaubey et al., 1990; Mukhopadhyay and Iyer, 1993; Parson et al., 1993; Briais, 1995; Mukhopadhyay et al., 1998; Mudholkar, 2001; DeMets et al. 2005), two distinct geomorphic and another two tectonic domains were demarcated along the SCIR stretch between latitudes 20°30'S and 23°07'S (study area, Figs. 1 and 2; Tables 1 and 2). Tectonically, the study area shows a combined characteristic of both slow spreading ridges (e.g., of Mid Atlantic Ridge) and fast spreading ridges (e.g., of East Pacific Rise; Mukhopadhyay and Iyer, 1993; Briais, 1995; DeMets et al., 2005). The geomorphic domains include Ridge-Crest-Floor-Valley (RCFV) and a Neo-Volcanic Zone (NVZ), while the tectonic domains include a Large Transform Discontinuities (LTD) and an Overlapping Spreading Center (OSC).

Geomorphic Domains: The approximately 300 km stretch of axial valley in the study area is deeper in excess of 3000 m in most places. The ridge segments are predominantly oriented NW-SE (140°-150° to 320°-330°) and show a pronounced axial valley (Fig.1). The depth of the axial valley ranges between little more than 2000 m to over 3500 (av. 3430 m). On average, the ridge axis at the shallower area shows least width (e.g., segment C). The width of the axial valley varies from 4 to 15 km (av. 10.9 km). The maximum relief within the valley floor is 900 m (range 500-1200 m) and height of the NVZ, wherever present, is about 266 m (range 200-500 m).

The segment A, on which sampling site 94 is located at 3318 m, remains fairly straight, with axial width varying between 4 and 15 km (narrow in north and wider towards south). The sampling site 93 is located on the inner valley flank of Segment B, which got shifted by the two large transform

discontinuities (D2 and D3) positioned on either side. The axial valley in segment B is quite wide by about 13 km. The segment C is characterized by narrow and relatively shallow axial valley. The entire segment appears to have been elevated owing probably to the effect of D3, a large transform discontinuity. Sampling was carried out from the inner flank of the axial valley in segment C (site 66). The relatively long segments D and E at their southern and northern end respectively curved to form the OSC between latitudes 21°20'S and 21°30'S. The axial valley along segment E was normally faulted in a series parallel to ridge axis all along the segment length, while such tectonic activities was largely absent along segment D. MORB rocks were dredged from the valley floor at sites 90 and 85 along the segment D. The valley floor is deeper (3500 m) in segment D compared to that of segment E (~ 3000 m). The segment F and H are quite long, interspaced by segment G and I of shorter length. The ridge crest along both the segment H and I were normally faulted towards axial valley.

The neo volcanic zone (NVZ) is bordered on the north by the GFZ (D9) and by D10 in the south (Fig. 1). The width of the ridge axial valley is highest in the NVZ area (~10 km). Sheet type aphyric basalts were dredged from the north-eastern and south-western slopes by almost the middle of the segment I, about 160 m above the floor bottom. Interestingly, vesicles on rocks are found filled with zeolites, the largest vesicle was measuring 2 x 20mm. The valley floor is about 6 km wide, and the mound type NVZ shows an elevation between 140 and 160 m. About 10 mm thick glassy veneer with few vesicles was encrusted at times by Fe-Mn oxides and clay.

Tectonic Domains: As many as nine well-developed ridge segments, separated by ten discontinuities, were encountered along the stretch of the study area (Table 1, see footnotes for type of discontinuities). The discontinuities intersect the ridge axis at an average spacing of about 42 km (range 16 to 62 km). It includes two major deviations of the ridge axis- at 20°32.5'S (Egeria TF / ETF) and at 22°45'S (Gemino FZ / GFZ). We also identified an Overlapping Spreading Centre (OSC) between 21°20'S and 21°30'S, a Neo-Volcanic Zone (NVZ) at 23°01'S, three Non-Transform Discontinuities (NTD, D4, D6 and D7) at 20°05'S, 21°40'S and 22°01'S, respectively. Two large (LTD- D2 at 20°54'S, and D3 at 20°58.5'S) and two moderate transform discontinuities (MTD- D8 at 22°12.5'S and D10 at 23°06'S were also encountered. While six discontinuities (D1, D3, D7 to D10) shifted the ridge segments located to their south towards west by about 1.2 to 21 km (av. 15.8 km), the three other discontinuities (D2, D4, and D6), on the contrary, shifted the ridge segments located to its south towards east by about 0.5 to 18 km (av. 6.7 km). The D5 represents the overlapping spreading centre.

The three discontinuities D4, D6 and D7 characteristically showed a negligible shift of the ridge axis. For example, the break between segments C and D along D4 is only 0.5 km, and that between segment E and F along D6 is only 1.85 km. The discontinuity D7 moved the segment G from segment F by only 1.2 km. The unusually low shift (av. 1.18 km) of segments along the discontinuities D4, D6 and D7 qualified them to be called as non-transform discontinuities (NTD).

The OSC occurs roughly between 21°20' S and 21°30.5'S and extends for 9.25 km in the north-south direction and 4 to 9 km in the east-west direction (Figs. 1 and 2). The detailed bathymetry of the OSC and probable evolution of the OSC with time is shown in Figure 2. The width between the northern and southern openings (between two arms) has been 2.85 km and 3.20 km, respectively. Towards the centre of the OSC, the sediment coverage reduces to less than 5% and occurs only as thin veneer on the rocky outcrops. Fresh, glassy, sheet lava occurs at the axial graben and also at the northern and southern tips of the arms, whilst older (?) pillow lavas occur within the OSC area. Fault scarps (~40 m relief) and talus are quite common. The OSC depicts a moderately steep (but devoid of steps) western flank and a rough and uneven eastern wall.

The multibeam bathymetry of the OSC (Fig. 2) shows the eastern wall losing its definite pattern of slope towards the south and tends to flatten a bit with a gradual increase in roughness (see Anon, 1987; Herzig and Plüger, 1988; Mukhopadhyay and Iyer, 1993; Briais, 1995). Based on the detailed study of the magnetic anomalies, Briais (1995) and Parson et al. (1993) modeled the development of the OSC (Fig. 2b). The model suggests that the axial segments D and E were continuous till 0.7 Ma ago, which however broke and separated by the discontinuity D5 by around 0.3 Ma, when the southern end of segment D curved and turned west, while the northern tip of segment E curved towards east. The OSC reached a seemingly matured stage by the present time.

Petrochemistry

Plagioclase and olivine generally dominate the phenocrystic assemblages in almost all the examined basalts in the study area. The plagioclase grains show a wide range in shape and size and vary from microlites in the groundmass having low anorthite content (probe analysis $An_{67.2}$, Herzig and Plüger, 1988), to large zoned plagioclase microphenocrysts with intermediate anorthite content ($An_{74.1}$). Olivine phenocrysts are forsteritic ($Fo_{84.7\text{-}89.6}$) while clinopyroxenes are rare. Several significant results emerged on correlating the major element chemistry (Tables 3 to 4, Fig.3).

The LTD and NVZ samples display further remarkable difference from OSC and RCFV samples with regard to their comparatively low CaO/TiO_2 and CaO/Al_2O_3 ratios (Tables 3 and 4, Fig. 3). The largely positive relation between Na_8 and $Fe_{8;}$ and seemingly weakly inverse relation between MgO

and TiO_2 and that between MgO and Na_2O/Na_2O+CaO suggest conformation of the studied samples to a local correlation trend. The samples from NVZ and LTD also show difference with strikingly high content of Nb, Sr and Ni and low Rb compared to rocks from the RCFV and OSC (Table 5).

The depth (Fe_8) and extent (Na_8) of melting, and fractionation index (Mg#) of the present suite of rocks also offer intriguing information about the behavior of the mother melts. For example, rocks from site 91 located on the LTD appears as relatively "primitive" (Mg# 63.02) while the Fe_8 (10.12) and Na_8 (2.62) values suggest its formation from a melt having limited extent of melting at a greater depth. The basalts from the NVZ (sites 87 and 88), on the other hand exhibit both fractionated and primitive characters (Mg # 61.70 and 64.40, respectively) and were perhaps produced at a great depth (Fe_8 9.59) from a low to moderately low extent of melting (Na_8 2.48). The basalts from the OSC (Sites 74, 77, 78, 80), however, show a relatively variable degree of fractionation (avg. Mg# 61.31-65.52), of a shallow melt characterized by higher degree of melting (8.72 and 2.15, respectively). Interestingly, the rocks from the geomorphic domain of RCFV show highly variable Mg# (58.64 to 65.59) including the most fractionated member with comparatively moderately high extent of melting (Fe_8 8.11) formed at a moderate depth (Na_8 2.49) (Tables 3 and 4, Fig. 3).

The isotopic ratio values of the SCIR samples (Fig. 4, Table 6) show lowest $^{87}Sr/^{86}Sr$ of 0.70282 at the Site 93 (in RCFV environment), which sharply increases to a highest value of 0.70371 at Site 91 at LTD, and a high value of 0.70309 at site 88 in a NVZ environment. In fact, compared to D2D and NVZ, the rocks from RCFV and OSC domains show low $^{87}Sr/^{86}Sr$ ratio (0.70282 to 0.70290). Similarly, the $^{206}Pb/^{204}Pb$ concentration has been markedly high in NVZ and LTD (18.453 and 18.412, respectively) compared to that in rocks from OSC and RCFV (18.01 at Site 74, 18.035 at Site 90, 18.057 at Site 93 and 18.16 at Site 94). Concentration of $^{207}Pb/^{204}Pb$ and $^{208}Pb/^{204}Pb$ are highest at Site 91 (15.518, 38.34, along LTD) and very high at Site # 87 (15.5, 38.368 in NVZ).

The relationship amongst the isotopic ratios of the studied rocks reveals some interesting results. In $^{207}Pb/^{204}Pb$ vs. $^{206}Pb/^{204}Pb$ binary plot, majority of the present data fall along or just above the northern hemisphere reference line (NHRL, Fig. 4). Samples from OSC are more akin to depleted mantle (DM) while samples from other two domains (NVZ and LTD) contain significant $^{207}Pb/^{204}Pb$ and $^{208}Pb/^{204}Pb$ for a given $^{206}Pb/^{204}Pb$ ratio (Fig. 4a, b). The samples from RCFV show intermediate $^{207}Pb/^{204}Pb$ and $^{208}Pb/^{204}Pb$ ratios. The enriched characters of NVZ and LTD samples are remarkably distinguishable in $^{87}Sr/^{86}Sr$ versus $^{206}Pb/^{204}Pb$ diagram (Fig. 4c). The present data along with published data from SCIR MORB occupy a distinct field as compared to Mid-Atlantic Ridge (MAR) and East Pacific Rise (EPR) data, however a few overlap exists. The sample from LTD (Site 91) plots outside any of these known fields, but close to the Mauritius and Reunion hotspot plume field

(Mahoney et al., 1992). Another noticeable fact is that in radiogenic Pb-Pb diagram, the SCIR MORB fall in a linear array just above the DM and Enriched Mantle (EM2) end member and resemble a linear mixing with Indian Ocean pelagic sediments (Fig. 4a, b). By contrast, the isotope data of IOTJ-MORB occupy a distinct field in the radiogenic Pb-Pb and Sr-Pb binary plots and invariably account for different mantle domains.

Discussion

A broad comparison of depth (Fe_8) and extent (Na_8) of melting, and fractionation index (Mg#) among the oceanic ridges of variable spreading rate, suggest that the fast spreading ridges (FSR) show extensive melting at great depth (e.g., the EPR with low Na_8 and highest Fe_8 (Niu and O Hara, 2008). In contrast, the slow spreading ridges (SSR) show low (less) melting at shallow to moderate depth (e.g., MAR with high Na_8 and moderate Fe_8), and sometimes moderate melting at shallow level (e.g., CIR with moderate Na_8 and lowest Fe_8, Langmuir et al., 1986; Batiza et al., 1988; Mukhopadhyay and Iyer, 1993). Again, it was found that the global correlation trend (GCT; where Na_8 and Fe_8 are inversely related, Klein and Langmuir, 1987) mostly occurs at the FSR (>60 mm/yr). In contrast, the local correlation trend (LCT, where Na8 and Fe8 values are fairly positively related, Niu and Batiza, 1993) occurs at the SSR (rate <50 mm/yr), while a combination of both can be seen at ridges spreading between 50 and 60 mm/yr (Mahoney et al., 1991; Lin and Phipps-Morgan, 1992). In this background, the petrochemical variations from 12 sites along the SCIR vis-à-vis tectonic and geomorphic conditions (Tables 1 to 6; Figs. 1 to 5) contribute to an understanding of the mechanism of formation, enrichment and ascent of the melt.

The relation between degree of fractionation and depth and extent of melting (Fig. 3) brought out interesting results from SCIR basalts. Most of the basalts from the RCFV domain have a range of Mg# (58-62) and a narrow range of Na_8 (2.1-2.4) and Fe_8 (8.5-9.5) except for some samples with Mg# >64 with higher Na_8 (3.2-3.4) and Fe_8 (>12.5). In comparison, the LTD basalts have a higher Mg# (62-64) and Na_8 (2.5-2.7) and Fe_8 (9.5-10). The OSC basalts have a slightly higher range of Mg# (61-64) and Na_8 (1.7-2.5) and Fe_8 (8-8.5). Interestingly, some of the OSC whole rock and glasses have high Mg# (>66) and Na_8 (>2.5) and Fe_8 (11.5). Most of the NVZ basalts, on the other hand, have a very narrow range of Mg# (61.5-62) and Na_8 (2.2-2.5) and Fe_8 (9-10) except for a few that have higher Mg# (64-65) but with similar Na_8 and Fe_8 values.

Our data from this stretch of slow to moderate spreading SCIR (Fig. 3; Tables 3 and 4) show a positive trend between Fe_8 and Na_8 values (i.e., low extent of melting occurring at great depth), suggesting short periods of melting during an initial phase at low temperature (Batiza et al., 1988).

The present dataset from the SCIR thus resembles more closely to the LCT model and confirms the concept of a fundamental difference in the dynamics of mantle upwelling beneath the SSR and FSR (Lin and Phipps-Morgan, 1992).

The above results suggest that in most cases the initial depths and extents of melting are similar for the basalts from the four tectonic domains but the final depth and degree of melting differed. This could be reconciled to the fact that the ascension of the melt through dikes, coupled with increased fractionation, occurs at the offsets due to the lowering of temperature. Our observations appear to be in conformity to the existing relation between volume and composition of melt with lithospheric extension (McKenzie and Bickle, 1988) and to the global correlations of ocean ridge basalt chemistry with axial depth (Niu and O'Hara, 2008). Incidentally, the rocks from site 66 (RCFV) display striking variation compared to other RCFV samples (Table 3, Fig 5), in terms of least fractionated mother melt (high pristinity / high fractionation index), even when the melt was appear to have formed at high depth with low extent of melting. The site 66 is located on segment C, which is characterized by a narrow but deep axial valley.

Slow to intermediate spreading ridges may often erupt enriched (E) and transitional (T) basalts along with depleted N-MORB. This is exemplified in Chile Ridge (Klein and Karsten, 1995), at north Juan de Fuca Ridge (Karsten et al., 1990) and at north EPR (Langmuir et al., 1990; Batiza et al., 1996). Considering Nb, Sr, V, Zr and Y contents (Table 5), most of the basalts from the SCIR (OSC, RCFV) are typical N-MORB, except for some from the NVZ (sites 87, 88) and LTD (site 91) (Table 6) that are isotopically similar to the T- or E-MORB (Subbarao et al., 1977; Dupre and Allegre, 1983; Le Roex et al., 1985; Mahoney et al., 1989).

The isotopic composition shows that the LTD basalts record highest $^{87}Sr/^{86}Sr$ ratio, while those from NVZ has highest ratios of lead isotopes ($^{206}Pb/^{204}Pb$, $^{207}Pb/^{204}Pb$, and $^{208}Pb/^{204}Pb$; Fig. 4, Table 6). The variable inputs of pelagic sediments probably resulted in higher radiogenic Pb values (Fig. 4b; cf. Ray et al., 2013). As compared to the other sites along the SCIR, the rocks from LTD and NVZ appear to have formed from a limited melt at a greater depth, largely remained pristine and are characterised by low CaO/Al_2O_3, CaO/TiO_2, high Nb, Sr and Ni, low Rb and high $^{87}Sr/^{86}Sr$, $^{206}Pb/^{204}Pb$, $^{207}Pb/^{204}Pb$ and $^{208}Pb/^{204}Pb$. These rocks are enriched in large-ion lithophile elements and may suggest a probable additional contribution from other source(s), as discussed later. In fact, the $^{87}Sr/^{86}Sr$ ratio in LTD basalt (site 91, 0.70371) is close to E-MORB of the MAR (0.70332; Hemond et al., 2006). The basalts at site 91 show enrichment only in isotopic character, but do not strikingly differ in major element compositions as compared to the other samples (Tables 3 and 4). A similar study correlating trace element and Pb isotope enrichment along 18° to 20°S was reported by Nauret

et al. (2006) for the MORB recovered between 18^{o} and 20^{o} S along the CIR. By contrast, Pb isotopic characters of the IOTJ basalts are more sensitive to depleted mantle (DM)-lower continental crustal mixing (Escrig et al., 2004; Ray et al., 2013).

The basalts from the NVZ (sites 87, 88) show striking variations in major and trace element chemistry as well as in isotope values (Tables 3 to 6). These basalts are relatively high in Na_8, Cr, $^{87}Sr/^{87}Sr$ and $^{206}Pb/^{204}Pb$ and $^{208}Pb/^{204}$ Pb than those from other sites, and are similar to T/E-MORB (Ray et al., 2013; Fig. 4). The presence of the Gemino FZ in the north might have created a conducive environment for the development of a melt enriched in incompatible elements probably through fractional crystallization. This is due to the fact that near the FZ the melt temperature reduces due to an increase in the percolation of cold seawater, causing large scale fractionation of the melt during its ascent.

Earlier investigations by Herzig and Plüger (1988), near the NVZ, reported a marginally high heat flow value of 2.4-4.4 heat flow unit (avg. 3.4 HFU) around the NVZ area, than the average values found along the CIR (1.4 HFU; 1988). Additionally, the total dissolved manganese and methane in the water column around the OSC area are 27.5 n.mol/kg and 45.6 nL/L, respectively. The discovery of massive sulfide-bearing hydrothermal field (and chimneys) just south of the NVZ location by RV Meteor and RV Sonne (also called as MESO zone) was extremely significant. The discovery of another hydrothermal plumes little north of the present suite of SCIR samples at 18°20'S and 9°30'S also recorded high CH_4/Mn (>6) and $CH_4/^3He$ (>60×10^6) ratios (Kawagucci et al., 2008). Keeping in mind the input of foreign material and hydrothermal fluid to the melt beneath the present area of investigation along the SCIR (specially at NVZ area), it was likely that such differential inputs have produced rocks of variable composition due to inefficient melt segregation and consequent re-equilibration of melt with the solid matrix. A subsequent reaction between the melt and the solid matrix during ascension may have dissolved pyroxene, precipitated olivine, and perhaps enhanced upwelling. The significance of hydrothermal inputs is discussed later.

All these indicate possible contribution or contamination from pelagic sediment to the ridge axis melt that produced the basalts at the LTD Site 91 (Rehkämper and Hofmann, 1997; Hofmann, 1997). While the input from low intensity circulating hydrothermal fluid (Herzig and Plüger, 1988, Halbach and Müench, 2000) might have modified the axial melt at the NVZ area (sites 87 and 88), and thus, making the rocks here distinctly different from the other CIR basalts. The isotopic data of basalts occurring at LTD and NVZ also suggest marginal contribution from lower mantle hotspot melt and circulating hydrothermal fluid, respectively. Furthermore, the SCIR rocks, in general, show a near-independent magmatic and tectonic segmentation, as their degree of fractionation and depth and

extent of melting (Mg#, Fe_8, and Na_8) do not exhibit wide variations (Table 3, Fig. 3). This suggests that larger magmatic segmentation may extend for several kilometres but may not necessarily correspond to tectonic segmentation. This is because the mantle compositional provinces may in some cases be larger than tectonically defined segments (Macdonald et al., 1984; Sinton et al., 1991). Nauret et al (2006) argues that the enrichment observed along the CIR axis is related to both the variable extent of melting and also could be due to probable plume-like influence. The narrow range of Na_8 content in the SCIR samples suggests that the observed compositional variations are related to enriched sources rather than only to low degrees of partial melting (McKenzie and Bickle, 1988; Niu et al. 2001).

The supply or ascension of melt to the ridge axis from a magma chamber at depth could normally be accomplished in two model-pathways - (a) through a simple central channel (Macdonald et al., 1984; Schouten et al., 1985), or (b) through multiple channels (Langmuir et al., 1986; Batiza et al., 1988). In the former model, basaltic magma chambers are envisaged as efficient mixing machines which buffer and homogenize the magma (O'Hara, 1985). The latter model, on the other hand, suggests the possibility of multiple injection channels of the melt from a variously fed, incompletely mixed, substantially zoned, and laterally heterogeneous magma chamber (Natland, 1980; Langmuir et al., 1986; Batiza et al., 1988).

The structural and geochemical data of the SCIR basalts from the present investigations are integrated to model the mechanism of ascension of melt at various sampling sites that represent different tectonic and geomorphic domains (Fig. 5). The trends of Na_8 and Fe_8 in the study area suggest generation of the melt due to moderate partial melting at greater depth and subsequent ascension through multiple injections (i.e., feeders / dikes) at various locations along the SCIR. Our data hint that the melt initially ascended by upwelling and was stored as PAMs (pockets of accumulated magma) located less than 5 km below the ridge crest (Fig. 5). The melt at the PAMs later underwent incubation, partial fractionation and enrichment by material from circulating hydrothermal fluids (in case of the NVZ) and by addition of material from ancient crust / plume material (in case of the LTD). Subsequently, the fractionated and, at places, enriched melt surfaced through dikes produced N-MORB (RCFV, OSC), T-MORM (LTD), and E-MORB (NVZ)

The prominent structural and magmatic entity in the study area is the OSC at 21°25'S. An OSC normally serves as a locus for the eruption of enriched, differentiated basalts and sometimes silicic rocks, and act as a region of independent magma supply (Macdonald, et al., 1984; Waters et al., 2011). However, the SCIR basalts (74, 77, 78 and 80) from the OSC area do not show major discernible deviations in major and trace elements, and also in isotopic compositions vis-à-vis the

basalts of the other locations along the SCIR (Tables 3 to 6). A comparable OSC along the Galapagos Spreading Centre in the Pacific Ocean displays significant variations in parental magma compositions and extent of low-pressure fractionation, small, discontinuous, or poorly mixed magma chambers. In contrast, the petrological and geochemical data indicate that the OSC along the SCIR to be characterized by a low melt supply (Rotella et al., 2009).

Conclusions

The geology and petrology of rocks from distinctly variable tectonic and geomorphic domains (LTD, OSC, NVZ and RCFV) along a nearly 300 km long stretch of the SCIR were investigated. The focus was to understand the formation, enrichment and ascension of the melt vis-à-vis different tectonic domains. The geochemistry of these rocks was correlated with the tectonic regimes of the area. The analyses of the rocks from 47 spots encompassing 12 sites and distributed over four characteristic geomorphic and tectonic domains suggest generation of melt by moderate degrees of partial melting at great depth. It seems that the magma ascended first to PAM, and subsequently through multiple injections (i.e., feeders / dikes) after being fractionated (at RCFV), and coupled with low overall melt supply (at OSC). There appears to be a marginal addition of lower mantle material or ancient oceanic crust / pelagic sediment (T-MORB at LTD), while hydrothermal fluid has enriched the basalts (E-MORB at NVZ).

Acknowledgements

This work was carried out under India's InRidge program and was supported by grants from the Office of Naval Research, ONR-USA (Grant N0014). The whole rock and glass were analyzed at the University of Hawaii. RM acknowledges the support of Rodey Batiza and to the late John J Mahoney during his stay at the SOEST, UH Manoa. We place on record our sincere thanks to one anonymous reviewer, Dr Brian Dreyer, and to Prof. Wolf-Christian Dullo, editor-in-chief, for their meticulous comments and guidance that helped immensely to improve the manuscript. This is NIO reference no.6860/14032013.

References

Anon 1987 Geothermal Metallogenesis in the Indian Ocean. Gemino Cruise Reports, SO 28, pp. 163

Armienti P, and Gasperini D, 2007 Do we really need mantle components to define mantle compositions? Journal of Petrology 48:693-709

Banerjee R, Iyer SD, 1991 Petrography and chemistry of basalts from the Carlsberg Ridge, Journal Geological Society of India 38:369-386

Batiza R, Niu Y, Karsten JL, Boger W, Potts E, Norby L, Butler R, 1996 Steady and non- steady state magma chambers below the East Pacific Rise. Geophysical Research Letters 23:221-224

Batiza R, Melson WG, O'Hearn T, 1988 Simple magma supply geometry inferred beneath a segment of the Mid-Atlantic Ridge. Nature 335:428-431

Briais A, 1995 Structural analysis of the segmentation of the Central Indian Ridge between 20°30'S and 25°30'S (Rodriguez Triple junction). Marine Geophysical Researches 17:431-467

Chaubey AK, Krishna KS, Subba Raju LV, Rao DG, 1990 Magnetic anomalies across the southern Central Indian Ridge: evidence for a new transform fault. Deep-Sea Research 37:647-656

DeMets C, Gordon RC, Royer J-Y, 2005 Motion between the Indian, Capricorn and Somalian plates since 20 Ma: implications for the timing and magnitude of distributed lithospheric deformation in the equatorial Indian Ocean. Geophysical Journal International 161:445-468

Drolia RK, Ghose I, Subramanyam AS, Malleswara Rao MM, Kessarkar P, Murthy KSR, 2000 Magnetic and bathymetric investigations over the Vema region of the Central India Ridge: Tectonic implications. Marine Geology 167:413-423

Dupre B, Allegre CJ, 1983 Pb–Sr isotope variation in Indian Ocean basalts and mixing phenomena. Nature 303:142-146

Engel CG, Fischer RL, 1975 Granitic to ultramafic rock complexes of the Indian Ocean ridge system, Western Indian Ocean. Bulletin Geological Society of America 86:1553-1578

Escrig S, Capmas F, Dupre B, Allegre CJ, 2004 Osmium isotopic constraints on the nature of the DUPAL anomaly from Indian mid-ocean-ridge basalts. Nature 431:59-63

Galer SJG, O'Nions RK,1989 Chemical and isotopic studies of ultramafic inclusions from the San Carlos volcanic field, Arizona: a bearing on their petrogenesis, Journal of Petrology 30:1033-1064

Gregg PM, Behn MD, Lin J, Grove TL, 2009 Melt generation, crystallization, and extraction beneath segmented oceanic transform faults. Journal of Geophysical Research 114:B11102, doi:10.1029/2008JB006100

Halbach P, Müench U, 2000 Mineral deposits at 23°S, Central Indian Ridge: mineralogical features, chemical composition, and isotopic investigations. In: Cronan, D., ed. Handbook of Marine Mineral Deposits, pp. 327-346

Hart SR, 1984 A large-scale isotopic anomaly in the Southern Hemisphere mantle. Nature 309:753-757

Hemond C, Hofmann AW, Vlastelic I, Nauret F, 2006 Origin of MORB enrichment and relative trace element compatibilities along the Mid-Atlantic Ridge between 10° and 24° N, Geochemistry Geophysics Geosystems 7, Q12010, doi:10.1029/2006GC001317

Herzig PM, Plüger WL, 1988 Exploration for hydrothermal mineralization near the Rodriguez Triple Junction, Indian Ocean. Canadian Mineralogist, 26:721-736

Hofmann AW, 1997 Mantle geochemistry: the message from oceanic volcanism. Nature 385:219-229

Iyer SD, Ray D, 2003 Structure, tectonic and petrology of mid-oceanic ridges and the Indian scenario. Current Science 85:277-289

Karsten JL, Delaney JR, Rhodes JM, Liias RA, 1990 Spatial and Temporal Evolution of Magmatic Systems beneath the Endeavour Segment, Juan de Fuca Ridge: Tectonic and Petrologic Constraints. Journal of Geophysical Research 95:19235-19256

Kawagucci S, Okamura K, Kiyota K, Tsunogai U, Sano Y, Tamaki K, Gamo T, 2008 Methane, manganese, and helium-3 in newly discovered hydrothermal plumes over the Central Indian Ridge 18°–20°S. Geochemistry Geophysics Geosystems, 9, Q10002, doi:10.1029/2008GC002082

Klein EM, Karsten JL, 1995 Ocean-ridge basalts with convergent-margin geochemical affinities from the Chile Ridge. Nature 374:52-57

Klein EM, Langmuir CH, 1987 Global correlations of ocean ridge basalt chemistry with axial depth and crustal chemistry. Journal of Geophysical Research 92:8089-8115

Langmuir CH, Bender JF, Batiza R, 1986 Petrological and tectonic segmentation of the East Pacific Rise, 5°30′–14°30′ N. Nature 322:422-429

Langmuir CH, Bender JF, Batiza R, 1990 A trace element enriched province on the East Pacific Rise north of the Orozco transform fault. Eos Trans. AGU, 71: 1703

Le Roex AP, Dick HJB, Reid AM, Frey FA, Erlank AL, Hart SR, 1985 Petrology and geochemistry of basalts from the American-Antarctic Ridge, Southern Ocean: implications for the westward influence of the Bouvet mantle plume. Contribution to Mineralogy and Petrology 90:367-380

Lin J, Phipps-Morgan J, 1992 The spreading rate dependence of three-dimensional mid-ocean ridge gravity structure. Geophysical Research Letters 19:13-16

Macdonald KC, Sempere JC, Fox PJ, 1984 East Pacific rise from Siqueiros to Orzoco fracture zone: Along strike continuity of axial neo-tectonic zone and structure and evolution of overlapping spreading centers. Journal of Geophysical Research 89:6049-6069

Mahoney JJ, Natland JH, White WM, Poreda R, Blommer SH, Fisher RL, Baxter A.N, 1989 Isotopic and geochemical provinces of the western Indian Ocean spreading centers. Journal of Geophysical Research 94:4033-4052

Mahoney JJ, Nicollet C, Dupuy C, 1991 Madagascar basalts: tracking oceanic and continental sources, Earth and Planetary Science Letters 104:350-363

Mahoney JJ, Le Roex AP, Peng Z, Fisher RL, Natland JH, 1992 Southwestern limits of Indian Ocean ridge mantle and the origin of low 206Pb/204Pb mid-ocean ridge basalt: Isotope systematics of the central Southwest Indian Ridge (17°–50°E). Journal of Geophysical Research 97:19,771-19,790

McKenzie D, Bickle MJ, 1988 The volume and composition of melt generated by extension of the lithosphere. Journal of Petrology 29:625-679

Melson WB, Vallier, TG, Wright, TL, Byerly G, Nelen J, 1976 Chemical diversity of abyssal volcanic glass erupted along Pacific, Atlantic, and Indian Ocean seafloor spreading centers. In: The Geophysics of the Pacific Ocean Basin, Geophys. Monograph series, v. 19: Washington (Am. Geophys. Union), p. 351-368

Mudholkar AV, 2001 Magmatic evolution of the fresh basalts from the Ridge axis near Egaria Fracture Zone, Central Indian Ridge. Journal Geological Society of India 58:329-339

Mukhopadhyay R, Iyer SD, 1993 Petrology of tectonically segmented Central Indian Ridge. Current Science 65:623-628

Mukhopadhyay R, Murthy KSR, Iyer SD, Rao MMM, Banerjee R, Subrahmanyam, AS, Shirodkar PV, Ghose I, 1998 InRidge program: Preliminary results from the first cruise. Current Science 75:1157-116

Natland JH, 1980 Effect of axial magma chambers beneath spreading centers on the compositions of basaltic rocks. In: Rosendahl, B. R., Hekinian, R., et al. (Eds.) Initial Reports. DSDP 54, Washington (U.S. Govt. Printing Office), 833-850

Nauret F, Abouchami W, Galer SJG, Hofmann AW, Hémond C, Chauvel C, Dyment, J, 2006 Correlated trace element-Pb isotope enrichments in Indian MORB along 18°–20°S, Central Indian Ridge, Earth and Planetary Science Letters 245:137-152 doi:10.1016/j.epsl.2006.03.015.

Niu Y, Batiza R, 1993 Chemical variation trends at fast and slow spreading ridges. Journal of Geophysical Research 98:7887-7902

Niu YL, O'Hara MJ, 2008 Global correlations of ocean ridge basalt chemistry with axial depth: A new perspective. Journal of Petrology 49:633-664

O'Hara MJ, 1985 Importance of the 'shape' of the melting regime during partial melting of the mantle. Nature 314:58-62

Othman DB, White WM, Patchett J, 1989 The geochemistry of marine sediments, island arc magma genesis and crust-mantle recycling. Earth and Planetary Science Letters 94:1-21

Parson LM, Patriat P, Searle RC, Briais AR, 1993 Segmentation of the Central Indian Ridge between $12^{o}12'$S and the Indian Ocean Triple Junction. Marine Geophysical Researches 15:265-282

Price RC, Kennedy AK, Riggs-Sneeringer M, Frey FA, 1986 Geochemistry of basalts from the Indian Ocean triple junction: implications for the generation and evolution of Indian Ocean ridge basalts. Earth and Planetary Science Letters 78:379-396

Purdy GM, Kong LSL, Christeson GL, Solomon SC, 1992 Relationship between spreading rate and the seismic structure of mid-ocean ridges. Nature 355:815-817.

Ray D, Iyer SD, Banerjee R, Misra S, Widdowson M, 2007 A petrogenetic model of basalts from the Northern Central Indian Ridge: 3°-11° S. Acta Geologica Sinica 81:99-112

Ray D, Banerjee R, Iyer SD, Mukhopadhyay S, 2008 A new report of serpentinites from Northern Central Indian Ridge (at 6^{o}S) – an implication for hydrothermal activity. Acta Geologica Sinica 82:1213-1222

Ray D, Misra S, Banerjee R, 2013 Geochemical variability of MORBs along slow to intermediate spreading Carlsberg-Central Indian Ridge, Indian Ocean. Journal of Asian Earth Sciences 70-71:125-141

Rehkamper M, Hofmann AW, 1997 Recycled ocean crust and sediment in Indian Ocean MORB. Earth and Planetary Science Letters 147:93-106

Rotella MD, Sinton JM, Mahoney JJ, Chazey III W, 2009 Geochemical evidence for low magma supply and inactive propagation at the Galapagos 93.25^{o}W overlapping spreading center. Geochemistry Geophysics and Geosystems, 10: Q09005, doi:10.1029/ 2009 GC002445

Schouten H, Klitgord KD, Whitehead JA, 1985 Segmentation of mid-ocean ridges. Nature 317:225-229

Sinton JM, Smaglik SM, Mahoney JJ, Macdonald KC, 1991 Magmatic processes at superfast spreading oceanic ridges: Glass compositional variations along the East Pacific Rise, 13^{o}–23^{o}S, Journal of Geophysical Research 96:6133- 6155

Subbarao KV, Hedge CE, 1973 K, Rb, Sr and $^{87}Sr/^{86}Sr$ in rocks from the Mid-Indian Oceanic Ridge**.** Earth and Planetary Science Letters 18:223-228

Subbarao KV, Reddy VV, Hekinian R, Chandrasekharam D, 1977 Large ion lithophile elements and Sr and Pb isotopic variations in volcanic rocks from the Indian Ocean. In: Indian Ocean Geology Biostratigraphy, Heirtzler, J.R., et al. (Eds.), American Geophysical Union, pp.259-278

Tapscott CR, Patriat P, Fisher RL, Sclater JG, Hoskins H, Parson B, 1980 The Indian Ocean Triple Junction. Journal of Geophysical Research 85:4723-4739

Waters CL, Kenneth WWS, Perfit MR, Blichert-Toft J, Blusztajn J, 2011 Perspective on the genesis of E-MORB from chemical and isotopic heterogeneity at 9-10 degrees N East Pacific Rise. Journal of Petrology 52:565-602

Captions to the Figures

Fig. 1. Simple tectonic fabric and axial bathymetry of the study area along the South Central Indian Ridge (SCIR), depicting a typical slow-to moderate spreading ridge axial valley. The thick NW-SE line is the ridge axis, comprising nine segments (A to I) separated by 10 discontinuities (D1 to D10). D1 is represented by Egeria Transform Fault in the north and D9 represents Gemino fracture Zone in the south. D2 and D3 discontinuities are large transform discontinuities (LTD), D8 and D10 are moderate transform discontinuities (MTD), while D4, D6 and D7 are non-transform discontinuities (NTD). Discontinuity D5 facilitates formation of overlapping spreading centre (OSC). See Table 1 footnotes for definition. Open circles with numbers along the ridge axis are sampling sites. The Indian Ocean Ridge System with study area in inset. Figure modified after Parson et al. (1993) and Briais (1995).

Fig. 2. **(a)** The detailed multibeam bathymetry of the Overlapping Spreading Centre occurring between 21°18'S and 21°30'S (courtesy SO-43 cruise). The width varies between 4 km (inner) and 9 km (outer). **(b)** The evolution of the OSC (after Briais 1995) suggests that segment D broke by discontinuity D5 at a low angle to give birth to a nascent OSC at about 0.3 Ma, which got matured by the present time.

Fig. 3. Eight binary plots of variation diagrams of selective major and trace elements of the SCIR rock from the study area, and also in relation to estimated depth (Fe_8), extent of melting (Na_8) and melt pristinity (fractionation index; Mg#). Both glass and whole rock analyses are presented geomorphic and tectonic domain-wise, along with those plotted from East Pacific Rise (EPR, Melson et al., 1976), Mid Atlantic Ridge (MAR, Melson et al., 1976), Carlsberg Ridge (CR, Banerjee and Iyer, 1991), Indian Ocean Triple junction (IOTJ, Price et al., 1986) and other reports from South Central Indian Ridge (Anon, 1987; Herzig and Plüger, 1988).

Fig. 4. Binary plots of present MORB data in $^{206}Pb/^{204}Pb$ versus (a) $^{207}Pb/^{204}Pb$, (b) $^{208}Pb/^{204}Pb$ and (c) $^{87}Sr/^{86}Sr$ diagrams along with mantle end members. Data Source: Atlantic and Pacific MORB: Petrological Database of Ocean floor. IOTJ: Price et al., 1986; Escrig et al., 2004, Literature data of SCIR: Rehkämper and Hofmann, 1997; Escrig et al., 2004, Indian Ocean Pelagic Sediments: Othman et al., 1989; Depleted mantle (DM): Hart, 1984; HIMU, EM1 and EM2: Armienti and Gasperini, 2007. Northern Hemisphere Reference Line (NHRL) from Hart, 1984.

Fig. 5. A cartoon (not to the scale) presenting a schematic framework of formation, enrichment and ascension of magma along the SCIR. The sample location, geological setting, structural discontinuities are shown, so also the fractionation index, water depth (bold line) and depth of melting (thin line) beneath sampling sites. Note that rocks from site 66 display striking variation compared to other RCFV samples. See text for details. PAM= Pockets of Accumulated Magma

Captions to the Tables

Table 1. Ridge segments and discontinuity characteristics along the SCIR.

Table 2. Location, geology and brief petrography of rocks at studied sites.

Table 3. Average major element composition (XRF) of the SCIR rocks.

Table 4. Average major element composition (microprobe analysis) of the SCIR glasses

Table 5. Trace element concentrations (ppm) of the SCIR basalts.

Table 6. Isotopic composition of basalts of the study area and those from other locations along the Central Indian Ridge

Supplementary Material

1. Supplementary to Table 3. Geochemical analyses of CIR whole rocks by XRF
2. Supplementary to Table 4. Geochemical analyses of SCIR Glasses by Microprobe

Fig 1

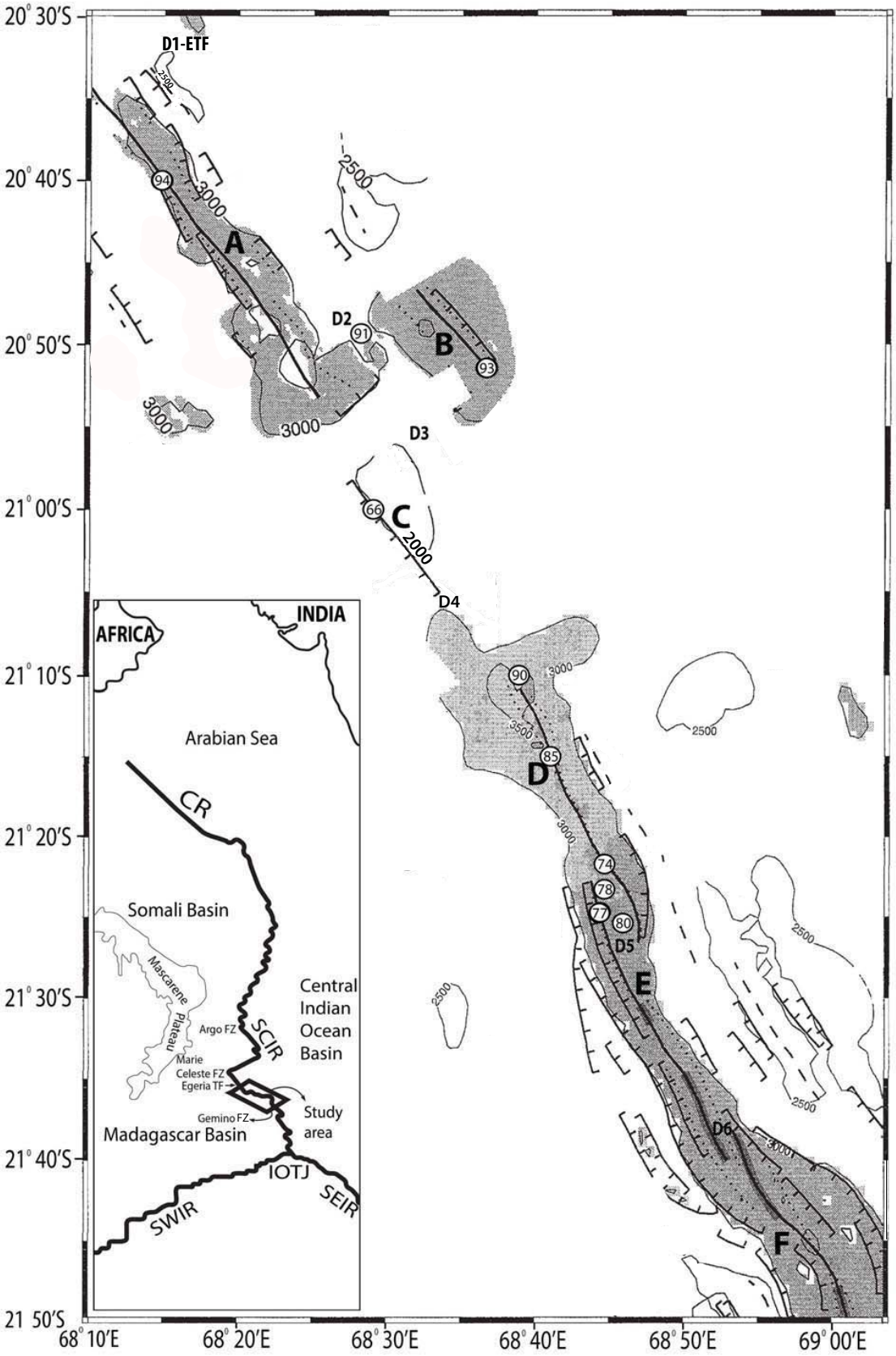
20° 30′S
20° 40′S
20° 50′S
21° 00′S
21° 10′S
21° 20′S
21° 30′S
21° 40′S
21 50′S
68° 10′E
68° 20′E
68° 30′E
68° 40′E
68° 50′E
69° 00′E
D1-ETF
D2
D3
D4
D5
D6
A
B
C
D
E
F
2500
3000
3500
2000
94
91
93
66
90
85
74
78
77
80
INDIA
AFRICA
Arabian Sea
CR
Somali Basin
Mascarene Plateau
Argo FZ
SCIR
Central Indian Ocean Basin
Marie Celeste FZ
Egeria TF
Gemino FZ
Study area
Madagascar Basin
IOTJ
SWIR
SEIR

(b)

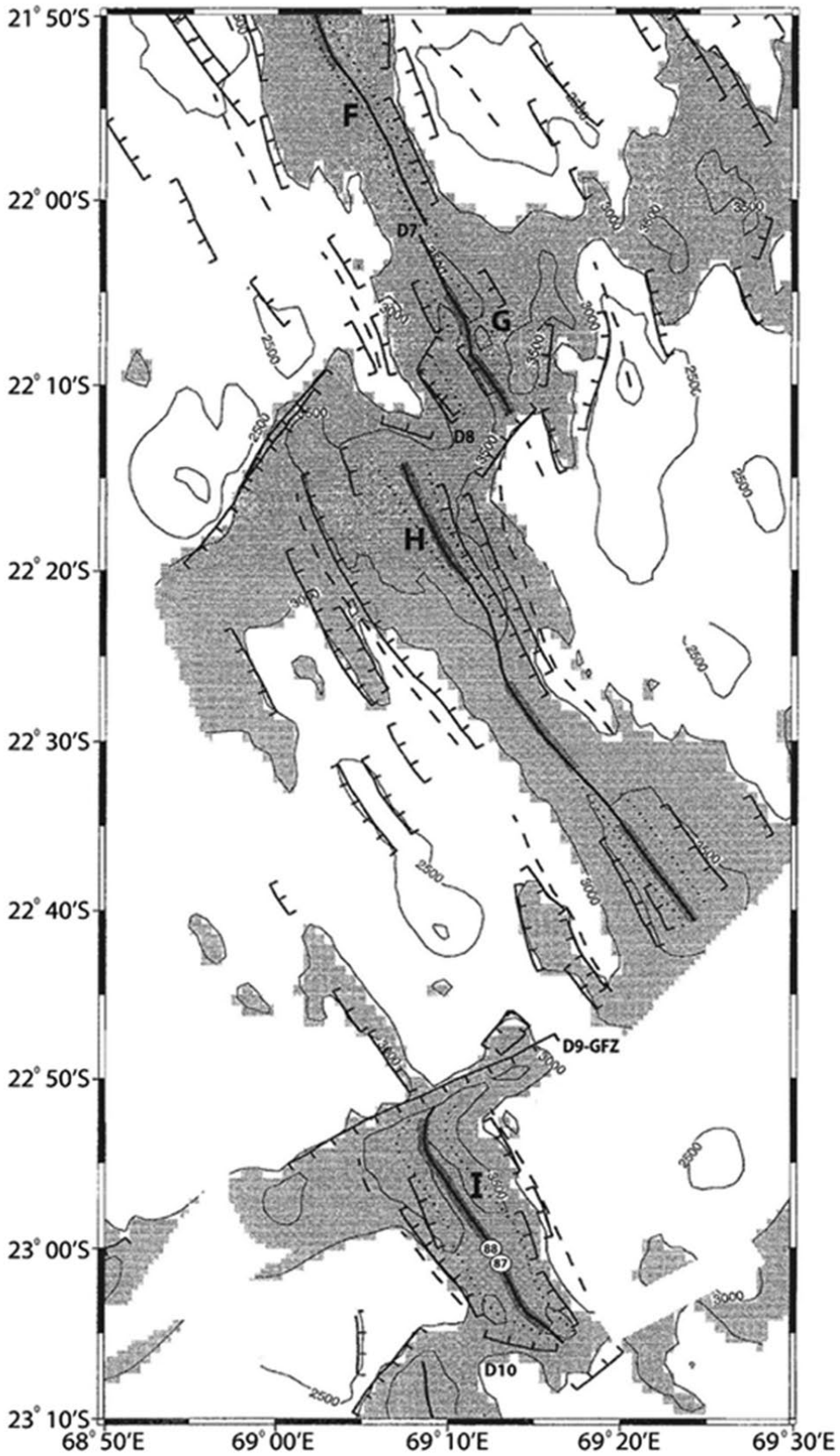
21° 50′S
22° 00′S
22° 10′S
22° 20′S
22° 30′S
22° 40′S
22° 50′S
23° 00′S
23° 10′S
68° 50′E
69° 00′E
69° 10′E
69° 20′E
69° 30′E
F
G
H
I
D7
D8
D9-GFZ
D10
68
67
2500
3000
3500

Fig 2(a)

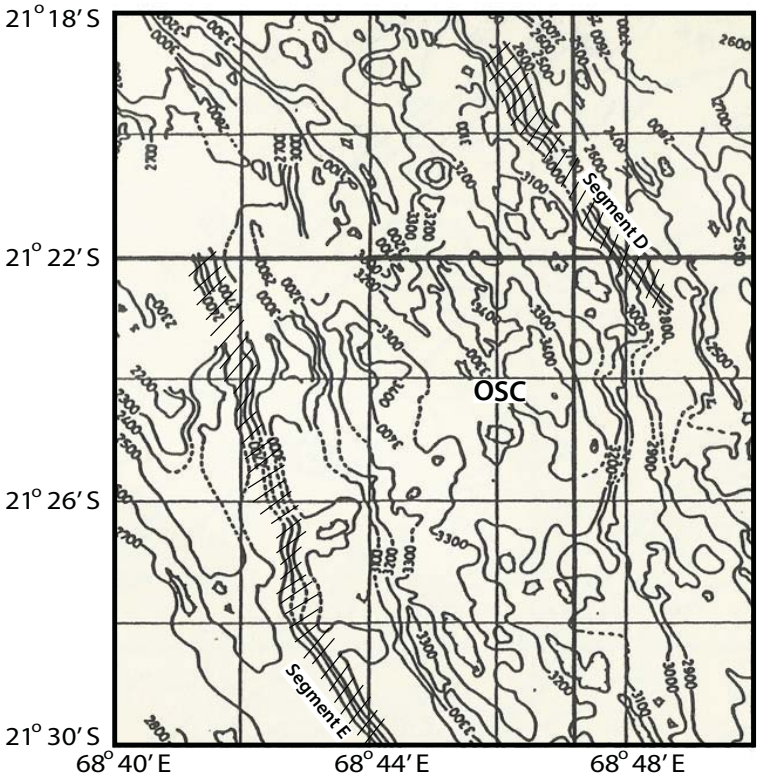
21° 18′ S
21° 22′ S
21° 26′ S
21° 30′ S
68° 40′ E
68° 44′ E
68° 48′ E
Segment D
Segment E
OSC

Fig 2(b)

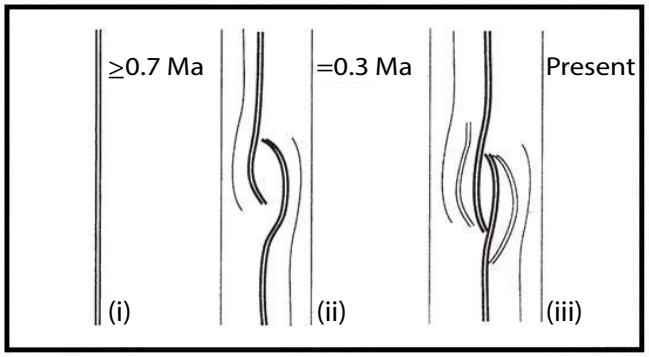
≥0.7 Ma
=0.3 Ma
Present
(i)
(ii)
(iii)

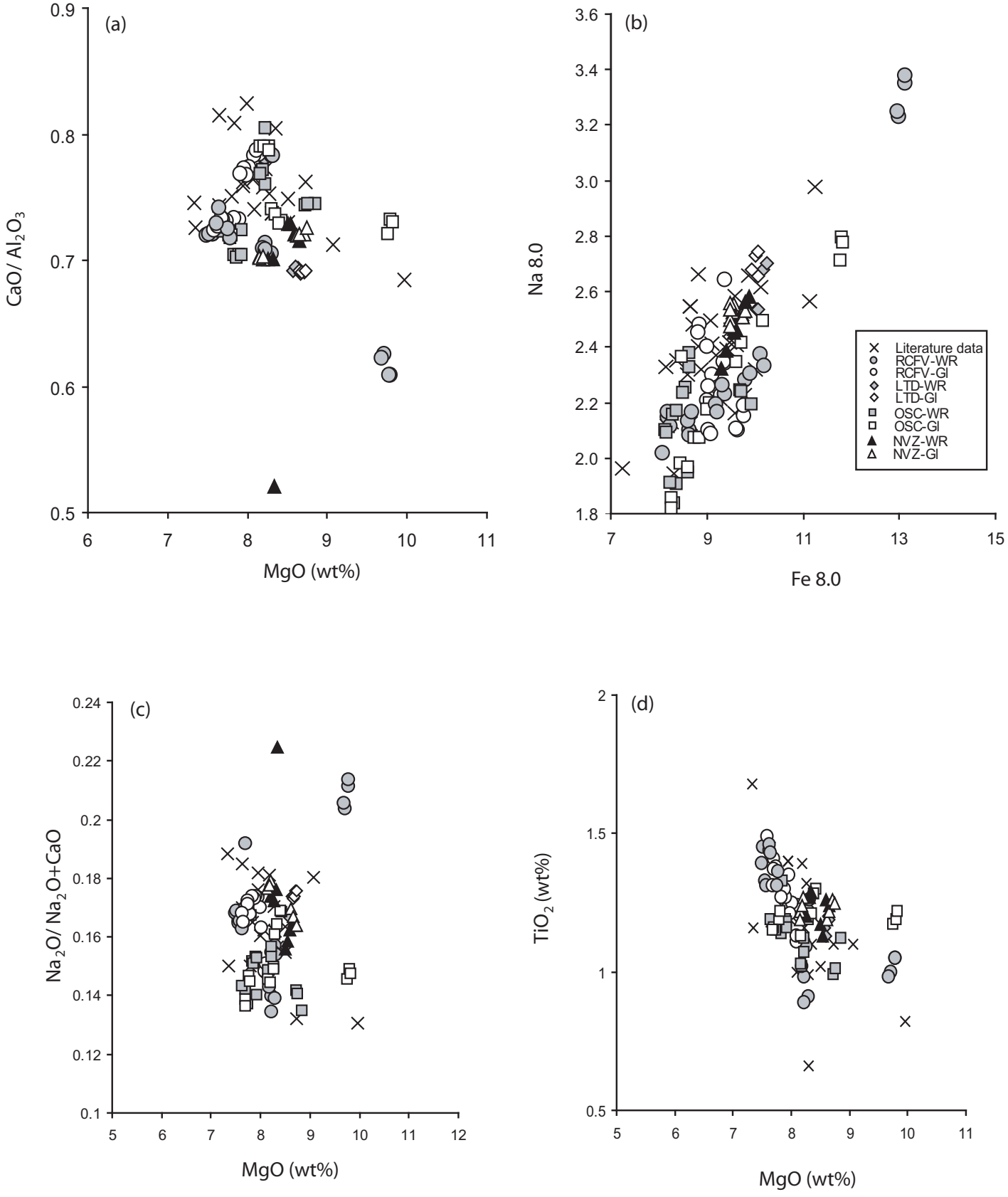
(a)
CaO/ Al2O3
MgO (wt%)
(b)
Na 8.0
Fe 8.0
Literature data
RCFV-WR
RCFV-GI
LTD-WR
LTD-GI
OSC-WR
OSC-GI
NVZ-WR
NVZ-GI
(c)
Na2O/ Na2O+CaO
MgO (wt%)
(d)
TiO2 (wt%)
MgO (wt%)

Fig 3 (a, b, c,d)

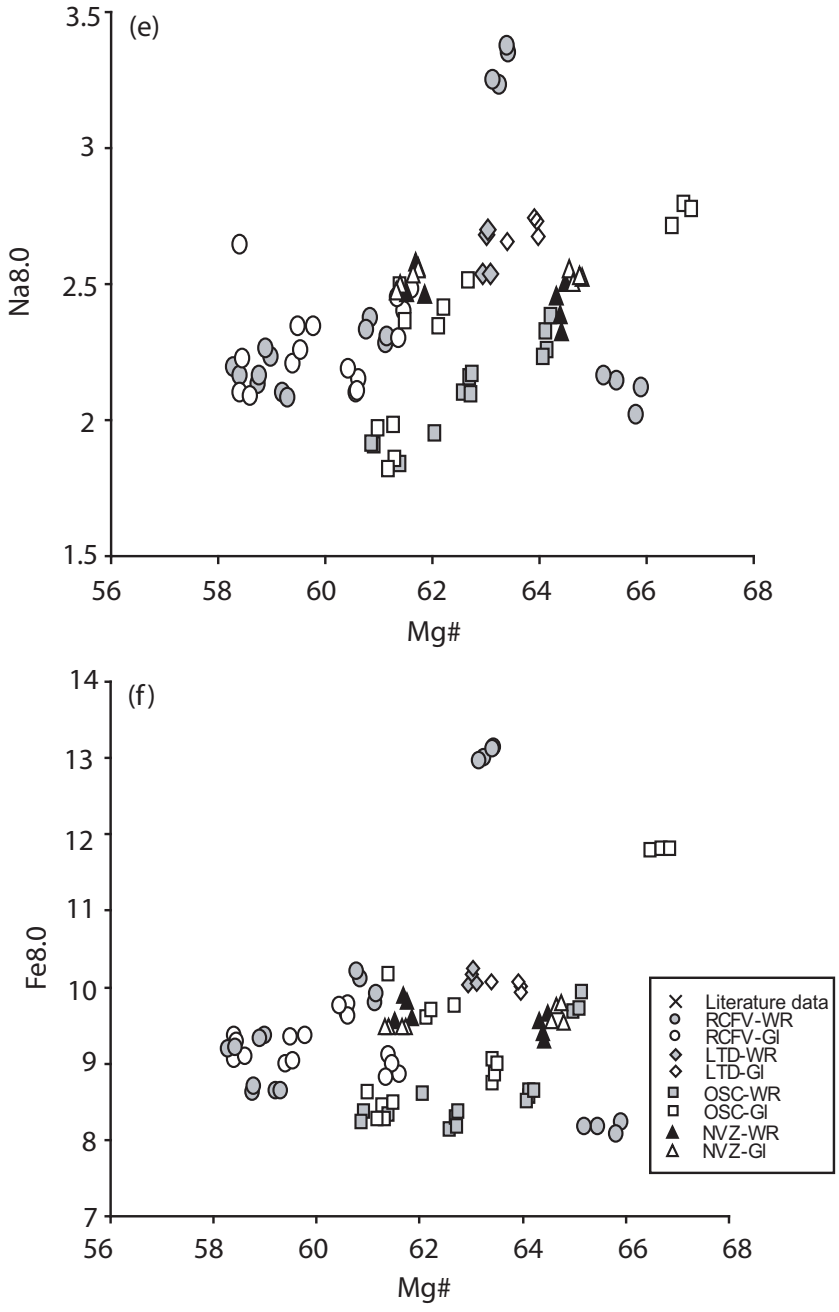
(e)
Na8.0
Mg#
(f)
Fe8.0
Mg#
Literature data
RCFV-WR
RCFV-GI
LTD-WR
LTD-GI
OSC-WR
OSC-GI
NVZ-WR
NVZ-GI

Fig 3 (e,f)

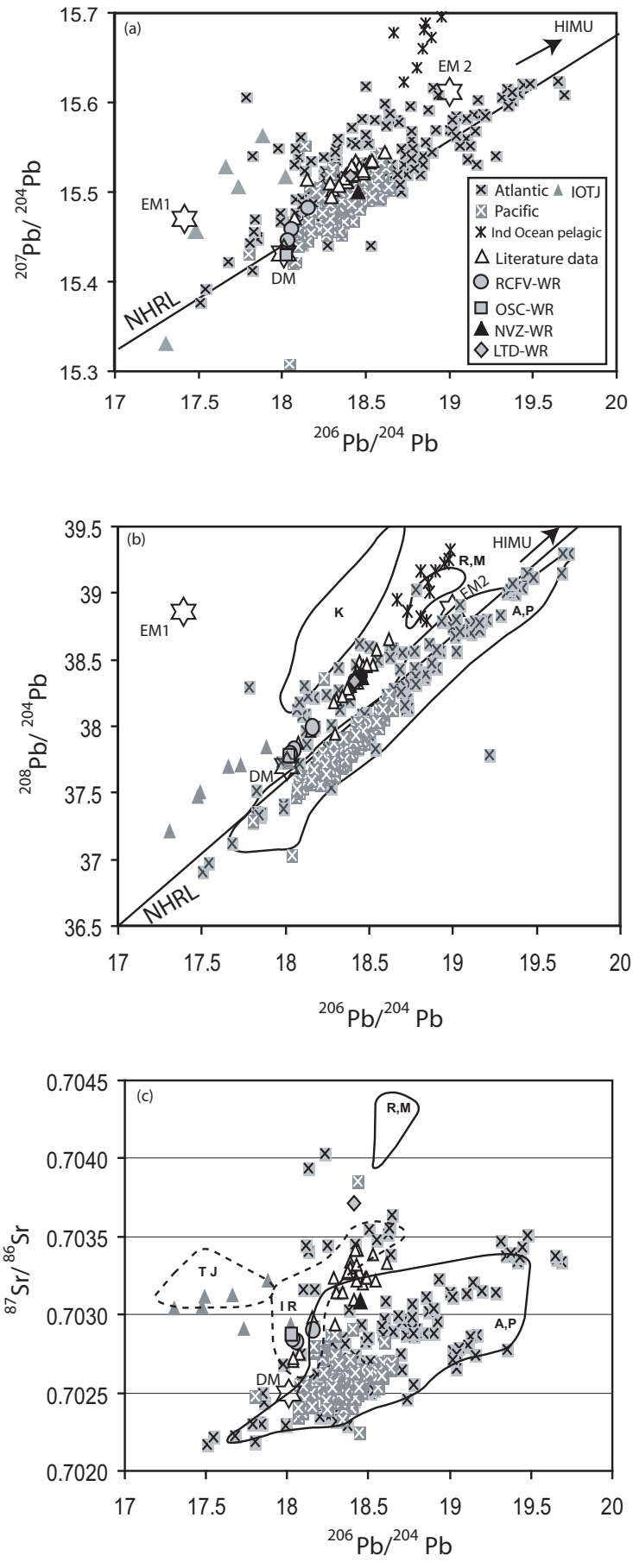
(a)
HIMU
EM 2
EM1
DM
NHRL
Atlantic
IOTJ
Pacific
Ind Ocean pelagic
Literature data
RCFV-WR
OSC-WR
NVZ-WR
LTD-WR
$^{207}Pb/^{204}Pb$
$^{206}Pb/^{204}Pb$
(b)
HIMU
R,M
EM2
K
A,P
EM1
DM
NHRL
$^{208}Pb/^{204}Pb$
$^{206}Pb/^{204}Pb$
(c)
R,M
T J
I R
A,P
DM
$^{87}Sr/^{86}Sr$
$^{206}Pb/^{204}Pb$

Fig 4

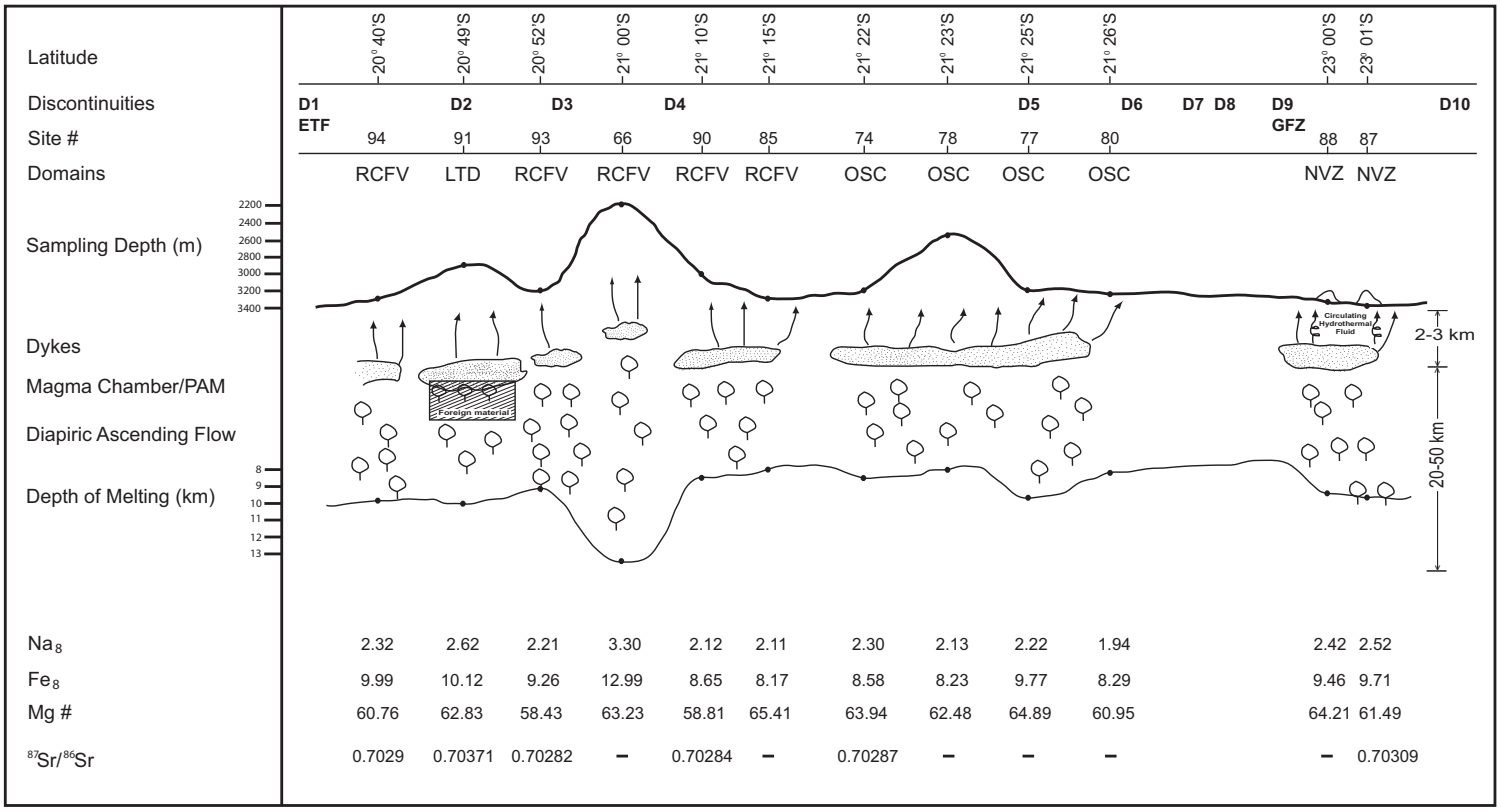
Latitude
20° 40'S
20° 49'S
20° 52'S
21° 00'S
21° 10'S
21° 15'S
21° 22'S
21° 23'S
21° 25'S
21° 26'S
23° 00'S
23° 01'S
Discontinuities
D1
D2
D3
D4
D5
D6
D7
D8
D9
D10
ETF
GFZ
Site #
94
91
93
66
90
85
74
78
77
80
88
87
Domains
RCFV
LTD
RCFV
RCFV
RCFV
RCFV
OSC
OSC
OSC
OSC
NVZ
NVZ
Sampling Depth (m)
2200
2400
2600
2800
3000
3200
3400
Dykes
Magma Chamber/PAM
Diapiric Ascending Flow
Depth of Melting (km)
8
9
10
11
12
13
Foreign material
Circulating Hydrothermal Fluid
2-3 km
20-50 km
Na8
2.32
2.62
2.21
3.30
2.12
2.11
2.30
2.13
2.22
1.94
2.42
2.52
Fe8
9.99
10.12
9.26
12.99
8.65
8.17
8.58
8.23
9.77
8.29
9.46
9.71
Mg #
60.76
62.83
58.43
63.23
58.81
65.41
63.94
62.48
64.89
60.95
64.21
61.49
87Sr/86Sr
0.7029
0.70371
0.70282
–
0.70284
–
0.70287
–
–
–
–
0.70309

Fig 5

Table 1. Ridge segments and discontinuity characteristics along the SCIR (north to south, between 20˚32' and 23˚06'S)

No	Segment		Axial Valley		Sampling Sites
	Trend	*Length, km*	*Width, km*	*Depth, m*	
A	145°	60	04-15	3000+	94
B	140°	16	13	2870, 3200	91 on LTD, 93
C	140°	21	06	2000+	66
D	140-145°	61	07-12	3500+	90, 85, 74,
E	145°	48	08	3000+	77, 78, 80
F	145°	60	14	3000+	---
G	144°	24	12	3000+	---
H	145°	62	15	3500+	---
I	150°	33	10	3500+	88, 87

Discontinuity Characteristics			
Name	**Location**	**Offsets (***Direction & approximate distance of Shift***)**	**Types**
D1	20° 32.5′	Segment A shifted to west by 15 km by Egeria TF	TF
D2	20° 54′	Segment B shifted to east 18 km	LTD
D3	20° 58.5′	Segment C shifted to west 21 km	LTD
D4	21° 05′	Segment D shifted to east by 0.5 km	NTD
D5	21° 25′	Overlapping Spreading Centre formed by segments D and E	OSC
D6	21°40	Segment F shifted to east by 1.85 km	NTD
D7	22° 01′	Segment G shifted to west by 1.2 km	NTD
D8	22° 12.5′	Segment H shifted to west by 11 km	MTD
D9	22° 45′	Segment I shifted to west by 33 km by Gemino FZ	FZ
D10	23° 06′	Following segment shifted to west by 13.5 km	MTD

Data of present study from four expeditions (Sonne-28 &43 and Sagar Kanya 16 & 20) were combined with those of Briais (1995), Parson et al., (1993), Herzig and Plüger (1988) and Rehkamper and Hofmann (1997). Ridge segments are often separated by discontinuity of < 2 km (non transform discontinuity= NTD), 2-10 km (small transform discontinuity= STD), 10-15 km (moderate transform discontinuity= MTD), 15-25 km (large transform discontinuity= LTD/ Transform Fault, TF) and > 25 km (Fracture Zone, FZ), OSC=Overlapping Spreading centre

Table 2. Location, geology and brief petrography of rocks from the Study Area, SCIR

Ridge Crest, Flanks, Valley (RCFV)	
94 20°39.6'S / 68° 14.8'E Depth 3318 m	~ 100 kg of fresh pillows recovered close to the valley floor in Segment A. Plagioclase phenocrysts (2-4 mm) are common
93 20°50.7'S / 68°28.1'E Depth 3200 m	About 80 kg of rocks (pillow + sheet) was recovered from Southern end of Segment B.
66 21°00'S / 68°29.3'E Depth 2200 m	Along undisturbed short ridge Segment C, Pillow and sheet lava recovered inside the axial valley.
90 21°10'S / 68°39.2'E Depth 3061 m	About 60 kg of sheet flow lava was recovered from the steep inner wall, about 489 m above the valley floor in Segment D. Plagioclase phenocrysts (5 mm) and large olivine crystals occur on 20 mm thick glass cover. Vesicles (<1 mm in dia) and 1-2 mm thick Fe-Mn coating present
85 21°14.9'S / 62°42.2'E Depth 3281 m	About 250 kg of pillow lava rocks was recovered from the valley floor of Segment D. The rocks are moderately phyric olivine-plagioclase basalts with 3 mm dia. plagioclase phenocrysts embedded in 15 mm thick glass, presence of FeMn veneer. A 231 cm long sediment core collected at 22^0S/68^0 31' E (3212 m) shows homogeneous light yellowish-brown calcareous clay.
Large Transform Discontinuity (LTD)	
91 20°49.8'S / 68° 29.9'E Depth 2870 m	About 20 kg of rocks recovered along Discontinuity D2, an LTD separates Segments A and B by 18 km. Both pillow and sheet lavas occur.
Over-Lapping Spreading Centre (OSC)	
74 21° 23.8'S / 68°44.9'E Depth 3198 m	About 400 kg of plagioclase phyric (sheet + pillow) basalts recovered from the eastern arm of the ridge, ~ 252 m above valley floor.
77 21° 25.7'S / 21°44.3'E Depth 3180 m	About 50 kg of rocks (sheet + pillow) dredged from the western arm of the ridge, about 270 m above the valley floor.
78 21° 23.5'S / 68°44.9'E Depth 2555 m	About 30 kg of plagioclase phyric pillows was recovered near the outer-crest of the western arm of the ridge. Plagioclase phenocrysts occur in the glass.
80 21° 25.5'S / 68°46.2'E Depth 3237 m	5 kg of pillows, plagioclase phyric variety rocks was recovered from the narrow bottom of the valley floor, having an extremely uneven steep inner walls, about 13 m above the floor. Plagioclase phenocrysts present in the glass.
Neo-Volcanic Zone (NVZ)	
88 23°00.8'S / 69°12.2'E Depth 3320 m	About 700 kg of sheet type aphyric basalt was recovered on the western inner wall of the axial valley, about 160 m above the floor bottom. The valley floor is about 6 km wide, with an elevation of 140 m at the centre which appears to represent neo-volcanic ridge. The glass is 2-5 mm thick and is overlain by Fe-Mn oxides and clay mineral. Vesicles are ~1 mm dia. and filled with zeolites (one vesicle is 2 x 20 mm).
87 23°01.6'S / 69°13.9'E Depth 3389 m	About 250 kg of aphyric basalt (sheet flow), was recovered close to the central elevated portion at the valley floor bottom (neo-volcanic ridge [?]). The glassy veneer (10 mm thick) with few vesicles, at times is encrusted by Fe-Mn oxides and clay.

Table 3. Average major element composition (XRF) of the SCIR rocks

RCFV						LTD
Sample No	**94A** (4)	**93A** (4)	**66A** (4)	**90A** (4)	**85A** (4)	**91A** (4)
SiO_2	49.88	51.22	48.41	50.85	50.46	49.42
TiO_2	1.17	1.39	1.02	1.37	0.95	1.17
Al_2O_3	15.43	15.78	16.33	15.9	17.63	16.71
Fe_2O_3	10.6	10.86	11.23	10.47	8.64	10.11
MnO	0.18	0.17	0.32	0.16	0.14	0.16
MgO	8.28	7.7	9.74	7.54	8.24	8.62
CaO	12.07	11.49	10.06	11.44	12.5	11.57
Na_2O	2.21	2.32	2.65	2.29	2.02	2.38
K_2O	0.2	0.09	0.14	0.08	0.07	0.04
P_2O_5	0.09	0.12	0.09	0.12	0.08	0.08
Total	**100.13**	**101.14**	**99.99**	**100.21**	**100.73**	**100.26**
FeO*	9.53	9.76	10.10	9.41	7.77	9.09
Na_8	2.32	2.21	3.30	2.12	2.11	2.62
Fe_8	9.99	9.26	12.99	8.65	8.17	10.12
Mg#	60.97	58.46	63.31	59.01	65.59	63.27
FeO*/MgO	1.15	1.27	1.04	1.25	0.94	1.05
CaO/Al_2O_3	0.78	0.73	0.62	0.72	0.71	0.69
CaO/TiO_2	10.32	8.27	9.86	8.35	13.16	9.88

OSC				NVZ	
74A (4)	**77A** (3)	**78A** (4)	**80A** (4)	**88A** (4)	**87A** (4)
50.98	50.27	50.5	50.13	50.51	50.2
1.06	1.04	1.16	1.17	1.2	1.25
16.25	16.07	17.19	16.77	15.89	16.23
9.17	9.42	9.38	9.78	9.47	10.28
0.15	0.15	0.15	0.15	0.15	0.16
8.2	8.78	7.88	7.7	8.57	8.28
12.41	11.96	12.1	12.15	11.5	11.39
2.22	1.93	2.17	2.05	2.2	2.41
0.09	0.04	0.1	0.07	0.28	0.2
0.08	0.08	0.1	0.1	0.14	0.13
100.62	**99.74**	**100.73**	**100.07**	**99.92**	**100.53**
8.24	8.47	8.43	8.79	8.51	9.24
2.30	2.22	2.13	1.94	2.42	2.52
8.58	9.77	8.23	8.29	9.46	9.71
64.14	65.52	62.69	61.31	64.40	61.70
1.01	0.96	1.07	1.14	0.99	1.12
0.76	0.74	0.70	0.72	0.72	0.70
11.70	11.54	10.43	10.43	9.58	9.11

$Na_{8.0}$ and $Fe_{8.0}$ are calculated for samples with 5.0 - 8.5 wt% MgO (following Klein and Langmuir, 1987). See text for formulae. The number of samples analyzed at each site is given within brackets.

Table 4. Average major element composition (microprobe) of the SCIR glasses

	RCFV				LTD
Sample No	**94B** (4)	**93B** (4)	**66B** (4)	**90B** (4)	**91B** (4)
SiO_2	49.68	51.12	50.76	50.88	49.48
TiO_2	1.17	1.4	1.27	1.34	1.17
Al_2O_3	15.23	15.75	15.29	15.51	16.68
Fe_2O_3	10.57	10.87	10	10.59	9.81
MnO	0.18	0.17	0.16	0.17	0.15
MgO	8.12	7.65	7.97	7.8	8.69
CaO	11.95	11.48	11.78	11.34	11.53
Na_2O	2.09	2.29	2.44	2.36	2.44
K_2O	0.18	0.08	0.15	0.08	0.03
P_2O_5	0.1	0.12	0.12	0.12	0.08
Total	**99.27**	**100.92**	**99.93**	**100.18**	**100.07**
FeO*	9.50	9.77	8.99	9.52	8.82
Na_8	2.14	2.16	2.43	2.29	2.70
Fe_8	9.70	9.19	8.94	9.19	9.97
Mg#	60.56	58.64	61.45	59.55	63.80
FeO*/MgO	1.17	1.28	1.13	1.22	1.01
CaO/Al_2O_3	0.78	0.73	0.77	0.73	0.69
CaO/TiO_2	10.21	11.54	9.28	8.46	9.85

	OSC				NVZ	
Sample Name	**74B** (4)	**77B** (4)	**78B** (4)	**80B** (4)	**88B** (4)	**87B** (4)
SiO_2	50.37	49.71	50.17	50.07	50.34	49.95
TiO_2	1.25	1.07	1.19	1.18	1.23	1.23
Al_2O_3	15.79	14.99	16.62	16.77	15.8	16.16
Fe_2O_3	10.09	9.48	9.8	9.76	9.48	10.22
MnO	0.16	0.15	0.15	0.16	0.15	0.16
MgO	8.37	8.23	7.79	7.75	8.68	8.17
CaO	11.58	11.83	12.06	12.13	11.4	11.34
Na_2O	2.3	2.04	2.08	1.99	2.27	2.45
K_2O	0.08	0.11	0.08	0.06	0.29	0.19
P_2O_5	0.11	0.1	0.1	0.1	0.14	0.12
Total	**100.10**	**97.72**	**100.04**	**99.97**	**99.8**	**100.01**
FeO*	9.07	8.52	8.81	8.77	8.52	9.19
Na_8	2.44	2.13	2.01	1.90	2.53	2.52
Fe_8	9.69	8.90	8.46	8.36	9.65	9.47
Mg#	62.11	63.45	65.32	61.24	64.68	61.52
FeO*/MgO	1.08	1.04	1.13	1.13	0.98	1.12
CaO/Al_2O_3	0.73	0.79	0.73	0.72	0.72	0.70
CaO/TiO_2	11.70	11.05	10.13	10.27	9.27	9.22

The number of samples analyzed at each site is given within brackets.

Table 5. Trace element concentrations (ppm) of the SCIR basalts.

Area >>	**RCFV**			**OSC**				**NVZ**	
Sample>>	**85**	**90**	**66**	**74**	**77**	**78**	**80**	**88**	**87**
Nb	1.90	1.40	1.30	1.15	1.30	1.40	1.05	7.10	5.10
Zr	73.90	86.80	Nd	75.20	74.50	65.80	74.10	84.10	86.10
Y	28.20	33.55	83.20	30	30.70	26.10	30.40	28.90	30
Sr	109.90	105.05	301.15	107.55	97.10	104.60	96.15	138.70	132.78
Rb	nd	nd	98.50	nd	nd	nd	0.60	4.60	3
Co	184	247.10	188.95	210.85	117	185.5	147.30	191.60	209.90
Mn	1285.75	1354.85	1316	1207.45	1255.85	1247	1247	1249.	1296.80
Cr	438.55	286.50	308.20	364.50	362.25	409.60	360.00	412.30	350.10
V	277	316	34.15	264.06	288.55	261.50	285.70	270.70	259.40
Zn	77	83.70	84.55	72.80	79	71.90	75.65	72.45	77
Cu	91.85	65	65.60	76.47	77.75	84.70	64.80	73.60	74.10
Ni	110.70	112.80	122	131.78	132.90	117.20	124.30	164	143.60

n.d.= not detected. Sr and Rb were measured by isotope dilution; uncertainties are estimated respectively at 0.4% and 1% or better.

Table 6. Isotopic composition of basalts of the study area and those from other locations along the Central Indian Ridge

Tectonic & Geomorphic domains and Sample sites		$^{87}Sr/^{86}Sr$	$^{206}Pb/^{204}Pb$	$^{207}Pb/^{204}Pb$	$^{208}Pb/^{204}Pb$
RCFV					
90		0.70284	18.035	15.446	37.783
93		0.70282	18.057	15.458	37.821
94		0.7029	18.16	15.482	37.986
OSC					
74		0.70287	18.028	15.429	37.772
NVZ					
87		0.70309	18.453	15.5	38.368
LTD					
91		0.70371	18.412	15.518	38.34
IOTJ					
12/16		0.70322	17.884	15.563	37.838
11/3		0.70304	17.307	15.531	37.214
104/21		0.70312	18.354	15.517	38.214
107/10-12		0.70305	17.955	15.491	37.916
SONNE-28					
46		0.702702	18.034	15.445	37.772
53		0.702752	18.074	15.471	37.879
71		0.702723	18.036	15.447	37.787
Indian MORB glasses					
On axis samples					
DR-03-2+		0.703319	18.4222	15.5195	38.3799
DR-03 1 vb		0.703144	18.3366	15.5075	38.2255
Gasitao samples					
DR04-4		0.703838	18.5832	15.5517	38.5321
DR07-1		0.703612	18.7927	15.5793	38.6938
DR08-1		0.703973	18.7465	15.5716	38.7042
DR09-1		0.703873	18.7041	15.5708	38.7304
DR10-1		0.703945	18.7031	15.5717	38.7377

Analysis courtesy: IOTJ= Indian Ocean Triple Junction (Subbarao and Hedge, 1973; Dupre and Allegre, 1983; Le Roex et al., 1985; Price et al., 1986; Mahoney et al., 1989, 1992). Sample 104-21 is from 19.83°S and 107/10-12 is from 24.35°S on the CIR (Mahoney et al. 1989); TJ 12-16 and TJ 11/3 are from the IOTJ (Price et al. 1986). Data from Rehkamper and Hofmann (1997) for SO-28 and SO-43 have also been incorporated for correlation. Indian MORB glasses taken from both on axis and Gasitao area (Nauret et al., 2006)

Supplimentary Tables

Supplementary to Table 3. Whole rock analysis of the SCIR basalts

	91				**94**				**85**				**93**				**90**			
	a	b	c	d	a	b	c	d	a	b	c	d	a	b	c	d	a	b	c	d
SiO2	49.45	49.38	49.53	49.32	49.53	50.27	49.37	50.36	50.58	50.36	50.53	50.37	51.37	51.03	51.27	51.11	50.72	50.96	50.81	50.91
TiO2	01.20	01.16	01.19	01.13	01.11	01.22	01.09	01.26	00.98	00.91	01.02	00.89	01.36	01.31	01.46	01.43	01.33	01.39	01.31	01.45
Al2O3	16.73	16.65	16.83	16.63	15.31	15.50	15.27	15.54	17.74	17.58	17.69	17.51	15.98	15.71	15.81	15.62	15.81	15.94	15.79	15.96
Fe2O3	10.13	10.09	10.16	10.06	10.47	10.68	10.51	10.74	08.68	08.59	08.74	08.55	10.82	10.82	10.91	10.89	10.42	10.52	10.39	10.55
MnO	00.17	00.13	00.18	00.16	00.06	00.26	00.13	00.27	00.17	00.09	00.19	00.11	00,27	00.09	--	00.15	00.16	00.17	00.13	00.18
MgO	08.63	08.57	08.66	08.60	08.23	08.30	08.27	08.32	08.22	08.30	08.19	08.23	07.78	07.75	07.62	07.65	07.56	07.49	07.57	07.52
CaO	11.60	11.52	11.61	11.55	11.97	12.14	12.01	12.16	12.66	12.39	12.54	12.41	11.47	11.38	11.53	11.58	11.40	11.47	11.38	11.51
Na2O	02.44	02.32	02.45	02.31	02.19	02.26	02.20	02.21	02.06	02.00	02.09	01.93	02.31	02.35	02.33	02.29	02.26	02.32	02.24	02.34
K2O	00.06	00.01	00.06	00.03	00.18	00.21	00.195	0.218	00.06	00.04	00.10	00.08	0.11	00.14	00.05	00.06	00.03	00.10	00.05	00.14
P2O5	00.10	00.09	--	00.08	00.03	00.11	00.06	00.16	00.06	00.08	00.07	00.11	00.10	00.07	00.16	00.15	00.10	00.13	00.08	00.17
Total	100.5	99.73	100.7	99.87	99.08	100.9	99.08	101.2	101.2	100.3	101.2	100.2	101.5	100.6	101.1	100.9	99.79	100.5	99.75	101.7

	66				**74**				**77**			**78**				**80**			
	a	b	c	d	a	b	c	d	a	b	c	a	b	c	d	a	b	c	d
SiO2	48.37	48.42	48.39	48.46	50.88	51.05	50.93	51.06	50.21	50.33	50.27	50.47	50.51	50.43	50.59	50.11	50.14	50.08	50.19
TiO2	01.00	01.05	00.98	01.05	01.02	01.07	01.03	01.12	00.99	01.12	01.01	01.14	01.19	01.33	01.18	01.15	01.18	01.16	01.19
Al2O3	16.21	16.44	16.27	16.40	16.19	16.28	16.21	15.32	16.05	16.14	16.02	17.16	17.20	17.18	17.22	16.73	16.84	16.71	16.80
Fe2O3	11.28	11.29	11.30	11.29	09.16	09.20	09.15	09.17	09.41	09.47	09.39	09.36	09.40	09.34	09.42	09.73	09.87	09.70	09.82
MnO	00.35	09.29	00.36	00.28	00.10	00.19	00.11	00.20	00.12	00.19	00.14	00.15	00.14	00.17	00.14	00.14	00.16	00.11	00.19
MgO	09.71	09.79	09.68	09.78	08.19	08.22	08.16	08.23	08.73	08.85	08.76	07.83	07.90	07.86	07.93	07.74	07.69	07.93	07.64
CaO	10.13	10.01	10.12	09.98	12.49	12.37	12.45	12.33	11.94	12.01	11.93	12.09	12.12	12.06	12.13	12.13	12.18	12.09	12.20
Na2O	02.59	02.68	02.62	02.71	02.18	02.24	02.17	02.29	01.97	01.87	01.95	02.16	02.19	02.14	02.19	01.93	02.02	01.97	02.04
K2O	00.13	00.16	00.09	00.18	00.07	00.11	00.06	00.12	00.01	00.09	00.02	00.11	00.07	00.12	00.10	00.05	00.10	00.03	00.06
P2O5	00.07	00.16	00.01	00.12	00.03	00.12	00.02	00.15	00.05	00.13	00.06	00.13	00.07	00.11	00.09	00.09	00.11	00.07	00.12
Total	99.84	100.3	99.82	100.2	100.3	100.8	100.3	99.99	99.48	100.2	99.54	100.6	100.8	100.7	100.9	99.80	100.3	99.85	100.2

	87				**88**			
	a	b	c	d	a	b	c	d
SiO2	50.13	50.19	50.22	50.26	50.57	50.48	50.56	50.43
TiO2	01.20	01.21	01.27	01.29	01.13	01.26	01.17	01.24
Al2O3	16.17	16.20	16.30	16.25	15.86	15.94	15.81	15.95
Fe2O3	10.19	10.26	10.31	10.36	9.45	09.53	09.40	09.53
MnO	00.13	00.14	00.18	00.19	00.13	00.19	00.12	00.16
MgO	08.26	08.20	08.32	08.34	08.54	08.59	08.51	08.65
CaO	11.33	11.35	11.42	08.46	11.56	11.49	11.53	11.42
Na2O	02.36	02.39	02.44	02.45	02.18	02.23	02.13	02.26
K2O	00.22	00.21	00.17	00.20	00.26	00.30	00.25	00.31
P2O5	00.10	00.11	00.14	00.17	00.12	00.17	00.13	00.14
Total	100.1	100.3	100.8	97.77	99.77	100.2	99.61	100.1

Supplementary to Table 4. Microprobe analysis of the SCIR basaltic glasses

	74				**77**				**66**				**90**				**93**			
	a	b	c	d	a	b	c	d	a	b	c	d	a	b	c	d	a	b	c	d
SiO2	50.31	50.42	50.33	50.42	49.68	49.79	49.66	49.71	50.66	50.88	50.72	50.80	50.97	50.82	50.93	50.80	51.06	51.25	51.19	50.98
TiO2	01.19	01.30	01.21	01.28	01.01	01.09	01.04	01.13	01.25	01.35	01.21	01.27	01.30	01.41	01.27	01.38	01.49	01.37	01.31	01.44
Al2O3	15.71	15.87	15.76	15.81	14.96	15.03	14.93	15.04	15.19	15.36	15.26	15.35	15.53	15.49	15.56	15.46	15.69	15.82	15.77	15.72
Fe2O3	10.12	10.04	10.14	10.56	09.42	09.55	09.45	09.50	10.09	09.92	10.02	09.97	10.62	10.54	10.68	10.52	10.81	10.97	10.92	10.78
MnO	00.11	00.20	00.15	00.18	00.19	00.20	00.09	00.18	00.09	00.26	00.11	00.17	00.24	00.09	00.22	00.13	00.16	00.19	0.22	00.11
MgO	08.30	08.43	08.35	08.40	08.16	08.28	08.21	08.27	08.02	07.96	07.99	07.91	07.89	07.71	07.84	07.74	07.59	07.70	07.68	07.63
CaO	11.63	11.60	11.61	11.52	11.82	11.87	11.79	11.84	11.75	11.87	11.71	11.79	11.37	11.29	11.40	11.30	11.36	11.58	11.56	11.42
Na2O	02.23	02.35	02.28	02.34	02.01	02.09	01.99	02.07	02.29	02.49	02.40	02.48	02.38	02.31	02.40	02.35	02.25	02.75	02.34	02.22
K2O	00.04	00.11	00.07	00.10	00.09	00.13	00.12	00.10	00.13	00.14	00.15	00.18	00.10	00.03	00.14	00.05	00.03	00.14	00.09	00.06
P2O5	0.13	0.11	0.09	--	00.08	00.13	00.06	00.13	00.16	00.10	00.13	00.09	00.09	00.14	00.12	00.13	00.07	00.18	00.14	00.09
Total	99.77	100.4	99.99	100.6	97.42	98.16	97.34	97.97	99.63	100.3	99.70	100.0	100.5	99.83	100.6	99.86	100.5	101.9	101.2	100.4

	91				**94**				**78**				**80**			
	a	b	c	d	a	b	c	d	a	b	c	d	a	b	c	d
SiO2	49.42	49.51	49.46	49.53	49.60	49.74	49.58	49.80	50.09	50.23	50.16	50.20	50.12	49.98	50.17	50.01
TiO2	01.16	01.19	01.15	01.18	01.11	01.20	01.13	01.24	01.17	01.19	01.18	01.22	01.16	01.19	01.15	01.22
Al2O3	16.63	16.70	16.66	16.73	15.16	15.27	15.21	15.28	16.67	16.55	16.68	16.58	16.75	16.79	16.73	16.81
Fe2O3	09.99	09.82	09.78	09.85	10.54	10.59	10.52	10.63	09.84	09.79	09.82	09.75	09.73	09.97	09.76	09.78
MnO	00.15	00.16	00.43	00.16	00.15	00.22	00.13	00.22	00.13	00.17	00.16	00.14	00.15	00.17	00.14	00.18
MgO	08.65	08.71	08.68	08.72	08.10	08.15	08.09	08.12	09.76	09.80	07.77	09.83	07.71	07.79	07.69	07.81
CaO	11.51	11.54	11.50	11.57	11.89	11.97	11.91	12.03	12.02	12.12	12.00	12.10	12.17	12.05	12.21	12.09
Na2O	02.41	02.46	02.42	02.47	02.06	02.09	02.07	02.14	02.05	02.12	02.06	02.09	01.96	02.04	01.93	02.43
K2O	00.02	00.04	00.01	00.05	00.16	00.21	00.13	00.22	00.06	00.11	00.07	00.08	00.05	00.04	00.05	00.10
P2O5	00.07	00.10	00.05	00.10	00.09	00.11	00.10	00.10	00.13	00.09	00.11	00.07	00.11	00.07	00.13	00.09
Total	100.0	100.2	100.1	100.4	98.86	99.55	99.87	99.78	101.9	102.2	101.0	102.1	99.96	100.1	99.96	100.5

	87				**88**			
	a	b	c	d	a	b	c	d
SiO2	49.90	49.99	49.87	50.04	50.33	50.39	50.29	50.35
TiO2	01.22	01.27	01.19	01.24	01.19	01.26	01.22	01.25
Al2O3	16.13	16.22	16.09	16.20	15.77	15.84	15.78	15.81
Fe2O3	10.25	10.17	10.27	10.19	09.47	09.53	09.40	09.52
MnO	00.15	00.19	00.13	00.17	00.15	00.12	00.15	00.18
MgO	08.15	08.20	08.14	08.19	08.62	08,71	08.65	08.74
CaO	11.34	11.37	11.29	11.39	11.35	11.42	11.38	11.47
Na2O	02.44	02.48	02.42	02.46	02.32	02.24	02.28	02.25
K2O	00.17	00.20	00.18	00.21	00.25	00.30	00.27	00.34
P2O5	00.14	00.11	00.11	00.12	00.11	00.15	00.14	00.16
Total	99.89	11.2	99.69	100.2	99.56	99.96	99.56	100.1